Journal Pre-proof

Thermodynamically consistent hydrodynamic phase-field computational modeling for fluid-structure interaction with moving contact lines

Qi Hong, Yuezheng Gong and Jia Zhao

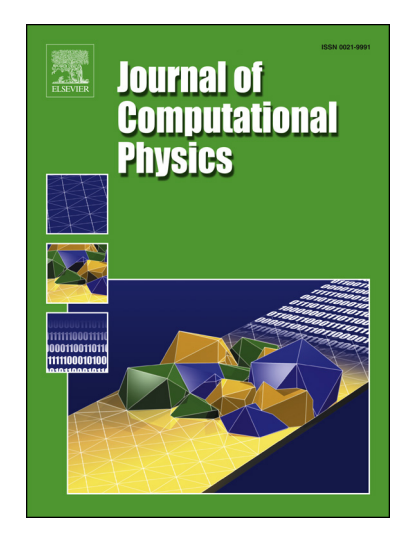
PII: S0021-9991(23)00504-1

DOI: https://doi.org/10.1016/j.jcp.2023.112409

Reference: YJCPH 112409

To appear in: Journal of Computational Physics

Received date: 11 January 2023 Revised date: 28 June 2023 Accepted date: 31 July 2023



Please cite this article as: Q. Hong, Y. Gong and J. Zhao, Thermodynamically consistent hydrodynamic phase-field computational modeling for fluid-structure interaction with moving contact lines, *Journal of Computational Physics*, 112409, doi: https://doi.org/10.1016/j.jcp.2023.112409.

This is a PDF file of an article that has undergone enhancements after acceptance, such as the addition of a cover page and metadata, and formatting for readability, but it is not yet the definitive version of record. This version will undergo additional copyediting, typesetting and review before it is published in its final form, but we are providing this version to give early visibility of the article. Please note that, during the production process, errors may be discovered which could affect the content, and all legal disclaimers that apply to the journal pertain.

© 2023 Published by Elsevier.

Journal Pre-proof

Highlights

- This paper proposes a novel computational modeling approach to investigate fluid-structure interactions with moving contact lines.
- By embracing the generalized Onsager principle and phase field method, the proposed PDE models are thermodynamically consistent and robust in investigating physical-relevant phenomena for fluid-structure interactions with moving contact lines.
- By introducing a novel supplementary variable, we transform the numerical scheme design problem into an optimization problem to which effective numerical techniques can be applied.
- Unlike many other schemes in the literature that respect a modified energy dissipation law, our proposed numerical method can indeed respect the original energy dissipation law.

Thermodynamically consistent hydrodynamic phase-field computational modeling for fluid-structure interaction with moving contact lines

Qi Hong¹, Yuezheng Gong¹, Jia Zhao^{2,*}

Abstract. This paper proposes a novel computational modeling approach to investigate the fluid-structure interactions with moving contact lines. By embracing the generalized Onsager principle, a coupled hydrodynamics and phase field system is introduced that can describe the fluid-structure interactions with moving contact lines in a thermodynamically consistent manner. The resulting partial differential equation (PDE) model consists of the Navier-Stokes equation and a nonlinear Allen-Cahn type equation. Volume conservation is enforced through an additional penalty term. A fully-discrete structure-preserving numerical scheme is proposed by combining several techniques to solve this coupled PDE system effectively and accurately. For the temporal discretization, we utilize the supplementary variable method for preserving the thermodynamic structure and the projection approach for reducing the problem size. Then, we use the finite difference method on the staggered grid for spatial discretization. Furthermore, we have rigorously proved that the proposed numerical scheme based on the second-order backward difference formula respects the original energy stability, i.e., the scheme is energy stable. Additionally, with the aid of the supplementary variable method, the resultant scheme can be transformed into a constrained optimization problem, where the solutions of the supplementary variables are the arguments of the objective function that reaches the optimality. Then the augmented Lagrangian method is introduced in part to bring robustness and efficiency to solving such a constrained optimization problem. Finally, various numerical simulations verify the model's capability and demonstrate the scheme's effectiveness, accuracy, and stability.

Key words: Phase-field, conserved Allen-Cahn, energy-stable, structure-preserving algorithm, supplementary Variable Method

1 Introduction

Many dynamical processes in scientific and engineering settings involve mixtures of multiple phases, for which the phase field method provides a state-of-the-art interface capturing approach [5,17,33,34,37,58,60]. Its primary advantage is that the evolving interface is retrieved intrinsically as a smooth solution of continuous PDEs instead of tracking it explicitly as other interface tracking methods. Moreover, the phase field method provides a practical and efficient approach in an Eulerian framework to simulate physical problems with interfaces.

The classical phase field models are the Cahn-Hilliard (CH) equation [5] and the Allen-Cahn (AC) equation [3]. The CH equation is usually used to model binary-fluid phase separations because it inherits the volume conservation, but it is relatively harder to solve numerically. The AC equation is more broadly used to describe the solidification and order-disorder

¹ School of Mathematics, Nanjing University of Aeronautics and Astronautics; Key Laboratory of Mathematical Modeling and High Performance Computing of Air Vehicles (NUAA); Ministry of Education Key Laboratory for NSLSCS, Nanjing, 211106, China.

² Department of Mathematics and Statistics, Utah State University, Logan, UT, 84322, USA.

^{*}Corresponding author. Email address: jia.zhao@usu.edu. (J. Zhao)

transitions of alloy systems. To describe the dynamics of the CH system in an arbitrarily complex domain, Kim et al. develop a modified CH system and further investigate its applications [25, 30, 42, 50]. The Allen-Cahn equation is a second-order equation, which is easier to compute numerically but does not conserve the volume of each phase. To circumvent this, Rubinstein et al. [36] introduced a nonlocal Allen-Cahn model with a nonlocal constraint to enforce volume conservation. After that, Brassel et al. proposed another strategy to preserve the conservation of volume [2]. By comparison, authors in [36] also suggested that the Allen-Cahn model with a volume constraint can serve as an alternative to the Cahn-Hilliard model for simulating interfacial dynamics of immiscible multi-component material systems.

When the hydrodynamic is considered, the velocity field shall be introduced, and its dynamics shall be properly coupled with the phase field variables. Meanwhile, the coupled system shall meet the thermodynamically consistent requirement to reflect the physics properly. Such hydrodynamic phase field models for multiphase fluids flows are usually derived by an energy variational approach [7,27,31,41,45,61]. The governing hydrodynamic phase field system naturally satisfies thermodynamics-consistent energy dissipation laws and is mathematically well-posed. The variational structure and thermodynamic property of the modeling approach have been exploited to develop structure-preserving numerical algorithms [22].

In the past few years, devising accurate, efficient, and structure-preserving numerical approximations for this type of this model has been an active field. There are many existing results in the literature on developing structure-preserving algorithms for solving thermodynamical and hydrodynamical phase-field models, including the convex splitting schemes [11, 14, 56], the stabilizer approach [29, 39, 47], exponential time differencing methods [15, 16], the fully-implicit structure-preserving schemes [1,48]. However, these popular approaches are not trivial to extend to hydrodynamic phase field systems for devising high-order schemes. Mainly, there are several difficulties: dealing with the nonlinear terms in the chemical potential, dealing with the coupling between the phase field and velocity field, and handling the nonlinear advection term in the Navier-Stokes equation. To decouple the incompressible Navier-Stokes equation and Cahn-Hilliard equation, one can use the operator splitting technique [20, 40, 59]. However, we emphasize that such decoupling is restricted to first-order accuracy in time due to the splitting error. How to design a second-order decoupling scheme for the hydrodynamic phase field model is still an open question. Recently, the energy quadratization approaches (such as IEQ, SAV, and their variants) provided a novel idea to develop some second-order accurate linear energy stable schemes [13,19,23,32,38,53]. And this idea has been further populated to investigate various hydrodynamic phase field models [32, 50–52, 54, 55]. Some work of the convergence analysis and error estimate for the phase-field-fluid coupled system can be found in [8–10, 18].

Although the phase field models for multiphase fluid problems, i.e., fluid-fluid interactions, and their numerical approximations are well studied, the extension for investigating fluid-structure problems, particularly fluid-solid interactions with moving contact lines, remain unresolved for a long time. Several major difficulties include describing the solid structure with a phase variable while respecting the variational structure, i.e., making sure the PDE model is thermodynamically consistent. Additionally, it is non-trivial to embed the moving contact line dynamics at the fluid-solid interface into the PDE model.

To address these issues, we introduce several techniques to develop a novel hydrodynamic phase-field computational model for fluid-structure interaction in complex domains with moving contact lines. A complex domain is modeled by a fixed phase field, which only depends on spatial variables. This system's total energy includes the kinetic and free energies of the fluid-fluid and fluid-solid interactions. On account of the contact angle, we add the contribution of the moving contact line energy at the fluid-solid boundary into the total free energy. To decrease the difficulties of solving the multiple coupled nonlinear fourth-order Cahn-Hilliard equations, we consider second-order Allen-Cahn dynamics, where the volume conservation for each phase is realized by introducing an additional penalty term. A thermodynamically consistent hydrodynamic phase-field model is then derived by the generalized Onsager principle in the presence of a two-phase incompressible Navier-Stokes flow. Subsequently, to develop an efficient numerical approximation that warrants the original physical structure, we first reformulate the system using constrained optimization supplementary variable method (SVM) fashion to construct a numerical scheme that warrants the original energy stable. We emphasize that the new SVM formulation is equivalent to the original system. And then, a fully discrete and decoupled energy stable numerical scheme is proposed to solve the newly developed hydrodynamical phase-field model in the irregular region, where the implicit-explicit BDF2 scheme and the staggered-grid finite difference method are utilized to discretize the governing system of equations in time and space, respectively. It is worth noting that the fully discrete BDF2 scheme is proven to warrant the original energy dissipation structure. To improve the computation of the supplementary variables at each time step, we adopt in this paper an augmented Lagrangian approach to develop an efficient algorithm for solving it. Their numerical results perform very well. In the end, some numerical examples and benchmark problems are calculated to verify the developed model's validity and effectiveness of the proposed numerical scheme.

The rest of the paper is organized as follows. In Section 2, we present a detailed derivation of the thermodynamically consistent hydrodynamical phase field model for fluid-structure interaction with moving contact lines. In Section 3, we introduce time-dependent supplementary variables to reformulate the original model into a constrained optimization problem. Then we propose a fully discrete and decoupled energy-stable scheme. The original energy dissipation is proved rigorously. Additionally, we use an augmented Lagrangian approach to solving the constrained optimization problem for supplementary variables. In Section 4, we present numerical results for various problems to validate the developed model's capability and our scheme's effectiveness. Some conclusions are given in Section 5.

2 Thermodynamically consistent phase-field model for fluid-structure interaction with moving contacting lines

Consider the computational domain $\Omega \in \mathbb{R}^d$, d = 2,3 smooth, open, rectangular, bounded, and connected. For any two matrix functions or 2nd order tensor functions \mathbf{F} , $\mathbf{G} \in L^2(\Omega)$, the inner product on Ω is denoted by $(\mathbf{F}, \mathbf{G}) = \sum_m \sum_n \int_{\Omega} \mathbf{F}_{m,n} \mathbf{G}_{m,n} d\mathbf{x}$, and the induced L^2 norm is given by $\|\mathbf{F}\| = (\mathbf{F}, \mathbf{F})^{1/2}$.

We briefly introduce the phase-field model for fluid-structure interaction (FSI) with a moving contact line (PF-FSI-MCL) in a viscous fluid matrix. Consider a two-fluid mixture with a third solid structure immersed. The volume fractions for fluid 1 and fluid 2 are denoted by $\phi_1(\mathbf{x},t)$ and $\phi_2(\mathbf{x},t)$ with the volume fraction for the solid structure denoted by $\phi_0(\mathbf{x})$, i.e., the solid-structure is time-independent. By incompressibility constraint, we shall have

$$\phi_0(\mathbf{x}) + \phi_1(\mathbf{x},t) + \phi_2(\mathbf{x},t) = 1, \forall (x,t) \in \Omega \times [0,T].$$

The volume-averaged density is $\rho := \rho_1 \phi_1 + \rho_2 \phi_2$ where ρ_1 and ρ_2 are the densities for fluid 1 and fluid 2. The volume-averaged viscosity is $\eta := \eta_1 \phi_1 + \eta_2 \phi_2$, where η_1 and η_2 are the viscosities for fluid 1 and fluid 2. For simplicity of notation, we use $\phi(\mathbf{x},t)$ to label the volume fraction of fluid 1. Thus, the volume fraction of fluid 2 can be retrieved as $1 - \phi(\mathbf{x},t) - \phi_0(\mathbf{x})$.

We assume the fluids are isothermal, incompressible, and have the same density. The fluid dynamics system is then governed by conservations of mass and momentum, i.e., the Navier-Stokes equation and the continuity equation in the domain Ω , as

$$\rho(\partial_t \mathbf{u} + \mathbf{u} \cdot \nabla \mathbf{u}) = -\nabla p + \nabla \cdot \boldsymbol{\tau} + \mathbf{F},\tag{2.1}$$

$$\nabla \cdot \mathbf{u} = 0, \tag{2.2}$$

where ρ is the volume-averaged density, \mathbf{u} is the volume-averaged velocity, $\boldsymbol{\tau} = 2\eta \mathbf{D}$ is the viscous stress tensor with the volume-averaged shear viscosity η and the strain rate tensor $\mathbf{D} = \frac{1}{2}(\nabla \mathbf{u} + \nabla \mathbf{u}^T)$, and \mathbf{F} is the external force.

The total free energy of the phase-field model for FSI with moving contact lines is postulated as follows

$$F[\phi,\phi_0] = F_{mix}[\phi] + F_{mcl}[\phi,\phi_0], \tag{2.3}$$

where $F_{mix}[\phi]$ is the well-known free energy for the binary fluid mixture in the phase-field framework, that described as

$$F_{mix}[\phi] = \int_{\Omega} \left(\frac{\gamma_1}{2} (1 - \phi_0) |\nabla \phi|^2 + f(\phi) \right) d\mathbf{x}, \tag{2.4}$$

where γ_1 is a parameter measuring the strength of the conformational entropy. One choice of the bulk energy density is the double-well potential $f(\phi) = \gamma_2 \phi^2 (1-\phi)^2$ with γ_2 measures the strength of the repulsive potential. In the sharp-interface limit, $\sqrt{\gamma_1 \gamma_2}$ is proportional to the surface tension, and $\varepsilon := \sqrt{\gamma_1/\gamma_2}$ measures the interfacial thickness. And the $F_{mcl}(\phi)$ is the moving contact line energy at the fluid-solid boundary [49], which is given by

$$F_{mcl}[\phi,\phi_0] = \gamma_3 \int_{\Omega} |\nabla \phi_0| g(\phi) \cos\theta d\mathbf{x}, \qquad (2.5)$$

where γ_3 controls contract angle strength, θ is the contact angle and $g(\phi)$ is a label function, with the properties g(1)=1, g(0)=-1, and g'(1)=g'(0)=0. So a reasonable choice would be $g(\phi)=6\phi^2-4\phi^3-1$. We again emphasize that $\phi_0(\mathbf{x})$ is the solid structure phase and independent of time. Its profile shall be $\tanh\frac{r(\mathbf{x})}{\sqrt{2}\varepsilon}$ with $r(\mathbf{x})$ as the distance of \mathbf{x} to the fluid-structure interface. By plugging in the initial profile of ϕ_0 into $|\nabla\phi_0|$, it is easy to verify that $|\nabla\phi_0|$ converges to a delta function at the fluid-structure interface as $\varepsilon\to 0$. Thus $|\nabla\phi_0|$ could be a good approximation for a delta function at the fluid-structure interface.

We define the volume for fluid 1 in the system as follows [26]

$$V(\phi) = \int_{\Omega} (1 - \phi_0) h(\phi) d\mathbf{x}, \qquad (2.6)$$

where $h(\phi)$ is a label function with the properties h(1) = 1, h(0) = 0 and h'(0) = h'(1) = 0. Thus, one could pick

$$h(\phi) := 3\phi^2 - 2\phi^3. \tag{2.7}$$

Note that when $h(\phi) = \phi$, it becomes the classical phase field definition for the volume of fluid 1. In reality, the volume $V(\phi)$ does not change during the evolution. To numerically enforce volume conservation, we introduce a large constant σ to penalize the volume derivation from the target volume $V_0:=V(\phi(x,y,t=0))$ in the free energy (2.3) so that the free energy is finalized as

$$F[\phi,\phi_0] = F_{mix}[\phi] + F_{mcl}[\phi,\phi_0] + \frac{\sigma}{2} (V(\phi) - V_0)^2, \qquad (2.8)$$

where σ is the penalizing parameter and a large positive constant. The reason for choosing $h(\phi)$ in (2.7) is to guarantee the penalization for volume derivation only occurs at the interface, but not in bulk, making it more physically meaningful.

This study assumes that the two fluid components have matching density and viscosity for simplicity. We will consider the scenario where they are different in subsequent studies.

Following the generalized Onsager principle [44], the PF-FSI-MCL hydrodynamics model ([30,50] and the references therein) reads as

$$\rho(\partial_t \mathbf{u} + B(\mathbf{u}, \mathbf{u})) = -\nabla p + \eta \Delta u - \phi \nabla \mu, \tag{2.9}$$

$$\nabla \cdot \mathbf{u} = 0, \tag{2.10}$$

$$\partial_t \phi + \nabla \cdot (\phi \mathbf{u}) = -\mathcal{M} \mu, \tag{2.11}$$

$$\mu = -\gamma_1 \nabla \cdot ((1 - \phi_0) \nabla \phi) + f'(\phi) + \gamma_3 g'(\phi) |\nabla \phi_0| \cos \theta + \sigma (1 - \phi_0) h'(\phi) (V(\phi) - V_0), \tag{2.12}$$

where $B(\mathbf{u},\mathbf{u}) = \frac{1}{2}(\mathbf{u}\cdot\nabla\mathbf{u} + \nabla\cdot(\mathbf{u}\mathbf{u}))$, and $\mathcal{M} \geq 0$ is a semi-positive definite operator known as the mobility. In the rest of this paper, we choose $\mathcal{M} := M(1-\phi_0)$ with $M \geq 0$ a constant, which ensures the dynamics occur outside of solid phase ϕ_0 . Note that we have recast the original convection term $\mathbf{u}\cdot\nabla\mathbf{u}$ in the momentum equation as $\frac{1}{2}[\mathbf{u}\cdot\nabla\mathbf{u} + \nabla\cdot(\mathbf{u}\mathbf{u})]$ thanks to the incompressible condition $\nabla\cdot\mathbf{u}=0$. This reformulation will be useful later for designing spatial structure-preserving numerical approximations. Here μ is the chemical potential that is calculated as the variational derivative of the free energy $\mu:=\frac{\delta F[\phi,\phi_0]}{\delta\phi}$.

The boundary conditions are not unique. Here, we consider the following physical boundary conditions

$$\mathbf{u}(\mathbf{x},t)|_{\partial\Omega} = \mathbf{0}, \, \partial_{\mathbf{n}}\phi|_{\partial\Omega} = 0, \tag{2.13}$$

where \mathbf{n} is the unit outward normal on the boundary. Note that this model may also adopt periodic-type boundary conditions for all variables. The initial conditions read as

$$\mathbf{u}(\mathbf{x},t=0) = \mathbf{u}^0, \, \phi(\mathbf{x},t=0) = \phi^0.$$
 (2.14)

The PF-FSI-MCL model (2.9)-(2.12) follows the law of energy dissipation, shown in the following theorem.

Theorem 2.1. The following energy law holds for the PF-FSI-MCL system (2.9)-(2.12)

$$\frac{\mathrm{d}}{\mathrm{d}t} \mathcal{E}[\mathbf{u}, \phi, \phi_0] = -\eta \|\nabla \mathbf{u}\|^2 - \left\| \sqrt{M(1 - \phi_0)} \mu \right\|^2, \tag{2.15}$$

where the total energy for this system is defined as

$$\mathcal{E}[\mathbf{u}, \phi, \phi_0] = \frac{\rho}{2} \|\mathbf{u}\|^2 + F[\phi, \phi_0]. \tag{2.16}$$

Proof. Firstly, taking the L^2 inner product of (2.9) with \mathbf{u} , using the integration by parts and applying the divergence-free condition (2.10), one can obtain

$$\frac{\rho}{2} \frac{\mathrm{d}}{\mathrm{d}t} \|\mathbf{u}\|^2 = -\eta \|\nabla \mathbf{u}\|^2 + (\nabla \cdot (\phi \mathbf{u}), \mu). \tag{2.17}$$

Taking the L^2 inner product of (2.11) with μ and performing integration by parts, it yields

$$(\partial_t \phi, \mu) + (\nabla \cdot (\phi \mathbf{u}), \mu) = -\left\| \sqrt{M(1 - \phi_0)} \mu \right\|^2. \tag{2.18}$$

Then one can take the L^2 inner product of (2.12) with $-\partial_t \phi$ and use the integration by parts once again, which leads to

$$(\mu, \partial_t \phi) = \frac{\gamma_1}{2} \frac{\mathrm{d}}{\mathrm{d}t} \int_{\Omega} (1 - \phi_0) |\nabla \phi|^2 \mathrm{d}\mathbf{x} + \frac{\mathrm{d}}{\mathrm{d}t} (f(\phi), 1) + \gamma_3 \frac{\mathrm{d}}{\mathrm{d}t} (g(\phi), |\nabla \phi_0| \cos \theta) + \frac{\sigma}{2} \frac{\mathrm{d}}{\mathrm{d}t} (V(\phi) - V_0)^2.$$

Finally, summing up the above with (2.17) and (2.18) immediately yields

$$\frac{\mathrm{d}}{\mathrm{d}t}\mathcal{E}[\mathbf{u},\phi,\phi_0] = -\eta \|\nabla \mathbf{u}\|^2 - \left\| \sqrt{M(1-\phi_0)}\mu \right\|^2 \le 0, \tag{2.19}$$

where the total energy for this system is

$$\mathcal{E}[\mathbf{u},\phi,\phi_0] = \frac{\rho}{2} \|\mathbf{u}\|^2 + F_{mix}[\phi] + F_{mcl}[\phi,\phi_0] + \frac{\sigma}{2} (V(\phi) - V_0)^2.$$
 (2.20)

The proof is complete.

3 Numerical approximation

One principle in developing numerical algorithms for solving the above PF-FSI-MCL system is to guarantee that the numerical solutions also satisfy the energy law in Theorem 2.1. Therefore, in the rest of this section, we will attempt to establish a second-order numerical scheme that follows the original energy law for this model.

3.1 Time discrete and original-energy stable scheme

In this subsection, we are now ready to develop a time-marching numerical scheme for the PF-FSI-MCL model. First of all, we introduce some notations for temporal discretization. Consider the time domain $t \in [0,T]$. We discretize it into equally distanced intervals $0 = t_0 < t_1 < t_2 < \cdots < t_{N_t} = T$ with $\delta t = T/N_t$. Let ϕ^n be the numerical approximation to the analytic function $\phi(\cdot,t_n)$.

Given $(\mathbf{u}^{n-1},\phi^{n-1})$ and (\mathbf{u}^n,ϕ^n) , and using a second-order implicit-explicit scheme based on Backward Difference Formula (BDF) and Adam-Bashforth method [4] for the time derivative, the numerical approximation for solving (2.9)-(2.12) reads as follows

$$\frac{a\phi^{n+1} - b\phi^n + c\phi^{n-1}}{2\delta t} + \nabla \cdot (\overline{\phi}^{n+1}\overline{\mathbf{u}}^{n+1}) = -M \cdot (1 - \phi_0)\mu[\phi^{n+1}, \overline{\phi}^{n+1}],\tag{3.1a}$$

$$\mu[\phi^{n+1}, \overline{\phi}^{n+1}] = -\gamma_1 \nabla \cdot ((1 - \phi_0) \nabla \phi^{n+1}) + f'(\overline{\phi}^{n+1}) + \gamma_3 g'(\overline{\phi}^{n+1}) |\nabla \phi_0| \cos \theta + \sigma (1 - \phi_0) h'(\overline{\phi}^{n+1}) \left(V(\overline{\phi}^{n+1}) - V_0 \right) + S(\phi^{n+1} - \overline{\phi}^{n+1}),$$
(3.1b)

$$\rho\left(\frac{a\widetilde{\mathbf{u}}^{n+1} - b\mathbf{u}^n + c\mathbf{u}^{n-1}}{2\delta t} + B(\overline{\mathbf{u}}^{n+1}, \overline{\mathbf{u}})\right) = -\nabla p^n + \eta \Delta \mathbf{u}^{n+1} - \phi^{n+1} \nabla \mu [\overline{\phi}^{n+1}, \overline{\phi}^{n+1}], \quad (3.1c)$$

$$\rho \frac{a(\mathbf{u}^{n+1} - \widetilde{\mathbf{u}}^{n+1})}{2\delta t} = -\nabla(p^{n+1} - p^n), \tag{3.1d}$$

$$\nabla \cdot \mathbf{u}^{n+1} = 0, \tag{3.1e}$$

where a = 3, b = 4, c = 1, the variable $\overline{(\bullet)}^{n+1} = 2(\bullet)^n - (\bullet)^{n-1}$ and S is a stabilizing constant. For this scheme, we have the following remarks.

Remark 3.1. In the above scheme, given the initial data for variables (\mathbf{u}^0, ϕ^0) at $t = t_0$, the second level values for variables (\mathbf{u}^1, ϕ^1) at $t_1 = \delta t$ can be achieved by the scheme (3.1a)-(3.1e) with a = b = 2, c = 0 and $\overline{(\bullet)}^{n+1} = (\bullet)^0$ in practice. This does not affect the overall accuracy of the second-order scheme (3.1a)-(3.1d).

Remark 3.2. With each time step, the scheme (3.1a)-(3.1e) entails the computation of velocity field and phase field by solving individual decoupled Helmholtz-type equation with a constant pre-computable coefficient matrix for each of these field variables. This leads to an efficient implementation of the scheme. However, it is non-trivial to prove its unconditional energy stable in theory.

Remark 3.3. If we replace all $\overline{(\bullet)}^{n+1}$ with $(\bullet)^{n+1}$, the pure second-order BDF2 scheme for this system (2.9)-(2.12) can be easily constructed. However, it is fully implicit and nonlinear, requiring the design of a nonlinear iteration solver to solve it. So it will yield a vast computational cost. Furthermore, it may not be provably unconditionally energy stable for all possible time step sizes. Therefore, developing a more convenient numerical scheme to solve this problem is necessary.

To modify the solutions of the scheme (3.1a)-(3.1e) owing the feature that respects the original energy dissipation law while maintaining both second-order accuracy and high efficiency, we utilize a novel stabilized supplementary variable method based on [19,23] to perturb the original governing system (2.9)-(2.12). Assuming that we have already obtained the solution of the original system up $t = t_n > 0$, we would like to find the solution up to $t_{n+1} > t_n$. To solve it, we introduce time-dependent supplementary variables $\alpha = (\alpha_1(t), \alpha_2(t))^T$ and reformulate the original model in $t \in (t_n, t_{n+1})$ into the following constrained optimization problem

$$\min_{\alpha_i} \omega_1 |\alpha_1|^2 + \omega_2 |\alpha_2|^2, \tag{3.2a}$$

s.t.
$$\phi_t + \nabla \cdot (\phi \mathbf{u}) = -M(1 - \phi_0)\mu + \alpha_1(t)h[\mathbf{u}, \phi],$$
 (3.2b)

$$\mu = -\gamma_1 \nabla \cdot ((1 - \phi_0) \nabla \phi) + f'(\phi) + \gamma_3 g'(\phi) |\nabla \phi_0| \cos \theta$$

+ $\sigma (1 - \phi_0) h'(\phi) (V(\phi) - V_0) + S(\phi - \phi),$ (3.2c)

$$\rho(\mathbf{u}_t + B(\mathbf{u}, \mathbf{u})) = -\nabla p + \eta \Delta \mathbf{u} - \phi \nabla \mu + \alpha_2(t) \mathbf{g}[\mathbf{u}, \phi], \tag{3.2d}$$

$$\nabla \cdot \mathbf{u} = 0, \tag{3.2e}$$

$$\frac{\mathrm{d}\mathcal{E}}{\mathrm{d}t} = -\eta \|\nabla \mathbf{u}\|^2 - \left\| \sqrt{M(1-\phi_0)}\mu \right\|^2,\tag{3.2f}$$

where ω_i , (i=1,2) are two weighting coefficients. In this paper, to facilitate the design of an efficient algorithm that decouples the computation of the pressure from that of the velocity, we set $\mathbf{g} = \rho \mathbf{u}$ in practice. Additionally, the choice of $h[\mathbf{u}, \phi]$ should include the penalty term to avoid breaking the volume constraint numerically. The reason for performing such a perturbation of the original model is that the solution $\boldsymbol{\alpha} = (\alpha_1(t), \alpha_2(t))^T = \mathbf{0}$, so this reformulation has not changed the original PDE system.

In the following, we will elaborate on the implicit-explicit BDF2 scheme for this system (3.2a)-(3.2f). Given $(\mathbf{u}^{n-1},\phi^{n-1})$ and (\mathbf{u}^n,ϕ^n) , we compute $(\mathbf{u}^{n+1},\phi^{n+1})$ via the following operation.

Scheme 3.1 (SSVM-BDF2).

$$\min_{\alpha_i^{n+1}} \omega_1 |\alpha_1^{n+1}|^2 + \omega_2 |\alpha_2^{n+1}|^2, \tag{3.3a}$$

s.t.
$$\frac{a\phi^{n+1} - b\phi^n + c\phi^{n-1}}{2\delta t} + \nabla \cdot (\phi_*^{n+1} \mathbf{u}_*^{n+1}) = -M(1 - \phi_0)\mu[\phi^{n+1}, \phi_*^{n+1}] + \alpha_1^{n+1}h[\mathbf{u}_*^{n+1}, \phi_*^{n+1}],$$
(3.3b)

$$\mu[\phi^{n+1},\phi_*^{n+1}] = -\gamma_1 \nabla \cdot ((1-\phi_0)\nabla\phi^{n+1}) + f'(\phi_*^{n+1}) + \gamma_3 g'(\phi_*^{n+1}) |\nabla\phi_0|\cos\theta + \sigma(1-\phi_0)h'(\phi_*^{n+1}) \left(V(\phi_*^{n+1}) - V_0\right) + S(\phi^{n+1} - \phi_*^{n+1}),$$
(3.3c)

$$\rho\left(\frac{a\widetilde{\mathbf{u}}^{n+1} - b\mathbf{u}^n + c\mathbf{u}^{n-1}}{2\delta t} + B(\mathbf{u}_*^{n+1}, \mathbf{u}_*^{n+1})\right) = -\nabla p^n + \eta \Delta \widetilde{\mathbf{u}}^{n+1} - \phi_*^{n+1} \nabla \mu_*^{n+1} + \alpha_2^{n+1} \mathbf{g}[\mathbf{u}_*^{n+1}],$$
(3.3d)

$$\rho \frac{a\mathbf{u}^{n+1} - a\widetilde{\mathbf{u}}^{n+1}}{2\delta t} = -\nabla(p^{n+1} - p^n), \tag{3.3e}$$

$$\nabla \cdot \mathbf{u}^{n+1} = 0, \tag{3.3f}$$

$$\frac{a\mathcal{E}^{n+1} - b\mathcal{E}^n + c\mathcal{E}^{n-1}}{2\delta t} = -\eta \|\nabla \mathbf{u}_*^{n+1}\|^2 - \|\sqrt{M(1 - \phi_0)}\mu_*^{n+1}\|^2, \tag{3.3g}$$

where $\mu_*^{n+1} = \mu[\phi_*^{n+1}, \phi_*^{n+1}]$. \mathbf{u}_*^{n+1} and ϕ_*^{n+1} follow the solutions of the time-marching scheme (3.1a)-(3.1e), and with the following boundary conditions

$$\mathbf{u}^{n+1}|_{\partial\Omega} = 0$$
, $\mathbf{n} \cdot \nabla \phi^{n+1}|_{\partial\Omega} = 0$. (3.4)

The following theorem shows the Scheme 3.1 satisfies the following property.

Theorem 3.1. The time-discrete SSVM-BDF2 scheme is energy stable in a sense that

$$\mathcal{E}^{n+1} \leq \mathcal{E}^n, \tag{3.5}$$

where the original energy \mathcal{E} at $t = t_n$ is defined as

$$\mathcal{E}^{n} = \frac{\rho}{2} \|\mathbf{u}^{n}\|^{2} + F_{mix}[\phi^{n}] + F_{mcl}[\phi^{n}, \phi_{0}]) + \frac{\sigma}{2} (V(\phi^{n}) - V_{0})^{2}.$$
(3.6)

Proof. It follows from (3.3g) with a = 3, b = 4, c = 1 that

$$\frac{3\mathcal{E}^{n+1} - 4\mathcal{E}^n + \mathcal{E}^{n-1}}{2} = \frac{3(\mathcal{E}^{n+1} - \mathcal{E}^n) - (\mathcal{E}^n - \mathcal{E}^{n-1})}{2} \le 0.$$
 (3.7)

Further, one can deduce

$$(\mathcal{E}^{n+1} - \mathcal{E}^n) \le \frac{1}{3} (\mathcal{E}^n - \mathcal{E}^{n-1}). \tag{3.8}$$

By the mathematical recursion, it yields

$$(\mathcal{E}^{n+1} - \mathcal{E}^n) \le \left(\frac{1}{3}\right)^n (\mathcal{E}^1 - \mathcal{E}^0). \tag{3.9}$$

On the other hand, since the first step is calculated by using the first-order scheme, we take n = 0 with a = b = 2 and c = 0 in (3.3g) to obtain

$$\mathcal{E}^1 - \mathcal{E}^0 \le 0. \tag{3.10}$$

Thus, substituting the above into (3.9) leads to

$$\mathcal{E}^{n+1} \leq \mathcal{E}^n, \tag{3.11}$$

which implies the conclusion and completes the proof.

Remark 3.4. It is noticed that another second-order numerical approximation based on the implicit-explicit Crank-Nicolson time-marching version follows the same line for solving this system (3.2a)-(3.2f). The details are omitted to save space. Interested readers are encouraged to explore the scheme.

Remark 3.5. We emphasize that in addition to the Crank-Nicolson scheme based on the Lagrange multiplier approach for solving phase-field model, the BDF2 scheme based on the Lagrange multiplier strategy still warrants a modified energy dissipation law other than the original energy law [13]. However, our decoupled scheme (3.3a)-(3.3g) proposed in this paper based on BDF2 can respect the original energy dissipation law, and the unconditional energy stability of the scheme is strictly proved in theory.

Remark 3.6. How to devise an efficient and original structure-preserving algorithm with the full decoupling structure and the second-order BDF2 scheme has always been a considerable challenge for the thermodynamically consistent phase-field method of fluid-structure interaction with moving contact lines. However, the idea of the SVM with a constrained optimization approach provides a new paradigm to develop original structure-preserving algorithms with great flexibility for devising solutions to this highly complex coupled nonlinear system.

3.2 Spatial discretization on staggered grids

Before developing the full-discrete scheme, we introduce some finite difference notations for spatial discretization. Although these notations can also be found in [12, 21, 46, 57], we summarize them in this part to make the paper reader-friendly.

Consider a rectangular spatial domain $\Omega = [0, L_x] \times [0, L_y]$ with L_x and L_y two positive numbers. The domain is discretized into uniform rectangular meshes with mesh size $h_x = L_x/N_x$ and $h_y = L_y/N_y$, where N_x and N_y are two positive integers. Consider the following four sets

$$E_x = \{x_{i+\frac{1}{2}} | i = 0, 1, \dots, N_x\}, \quad E_{\bar{x}} = \{x_{i+\frac{1}{2}} | i = -1, 0, \dots, N_x + 1\},$$
 (3.12)

$$C_x = \{x_i | i = 1, 2, \dots, N_x\}, \qquad C_{\bar{x}} = \{x_i | i = 0, 1, \dots, N_x + 1\},$$
 (3.13)

where $x_i = (i - \frac{1}{2})h_x$. Here E_x and $E_{\bar{x}}$ are called the uniform partition of $[0, L_x]$ into N_x equally-sized intervals, and its elements are called edge-centered points. The two points belonging to $E_{\bar{x}} \setminus E_x$ are called ghost points. The elements of C_x and $C_{\bar{x}}$ are called cell-centered points. Again, the two points belonging to $C_{\bar{x}} \setminus C_x$ are called ghost points. Analogously, the sets E_y and $E_{\bar{y}}$ contain the edge-centered points, and C_y and $C_{\bar{y}}$ contain the cell-centered points of the interval $[0, L_y]$.

Define the following discrete functions spaces

$$C_{x \times y} = \{ \phi | C_x \times C_y \to \mathbb{R} \}, \quad C_{\bar{x} \times y} = \{ \phi | C_{\bar{x}} \times C_y \to \mathbb{R} \}, \quad C_{x \times \bar{y}} = \{ \phi | C_x \times C_{\bar{y}} \to \mathbb{R} \}, \quad (3.14)$$

$$\mathcal{C}_{\bar{x}\times\bar{y}} = \{\phi|C_{\bar{x}}\times C_{\bar{y}}\to\mathbb{R}\}, \quad \mathcal{E}^{ew}_{x\times y} = \{u|E_x\times C_y\to\mathbb{R}\}, \quad \mathcal{E}^{ew}_{x\times\bar{y}} = \{u|E_x\times C_{\bar{y}}\to\mathbb{R}\}, \quad (3.15)$$

$$\mathcal{E}_{x \times y}^{ns} = \{ v | C_x \times E_y \to \mathbb{R} \}, \quad \mathcal{E}_{\bar{x} \times y}^{ns} = \{ v | C_{\bar{x}} \times E_y \to \mathbb{R} \}, \quad \mathcal{V}_{x \times y}^{vc} = \{ f | E_x \times E_y \to \mathbb{R} \}, \quad (3.16)$$

for cell-centered functions, east-west edge-centered functions, north-south edge-centered functions, and vertex-centered functions, respectively. For simplicity, we introduce several average and difference operators

edge to center average and difference operators:
$$a_x$$
, a_y , d_x , d_y , (3.17)

center to edge average and difference operators:
$$A_x$$
, A_y , D_x , D_y , (3.18)

vertex to edge average and difference operators:
$$\mathfrak{a}_x$$
, \mathfrak{a}_y , δ_x , δ_y , (3.19)

edge to vertex average and difference operators:
$$A_x$$
, A_y , D_x , D_y , (3.20)

and also define an average operator **A** such that $\mathbf{A}\phi = \begin{pmatrix} A_x\phi & 0 \\ 0 & A_y\phi \end{pmatrix}$ and some discrete divergence operators

$$\nabla_d = (d_x, d_y)^T, \quad \nabla_D = (D_x, D_y)^T, \quad \nabla_{(d, \mathcal{D})} = (d_x, \mathcal{D}_y)^T, \tag{3.21}$$

$$\nabla_{(D,\delta)} = (D_x, \delta_y)^T, \quad \nabla_{(\mathcal{D},d)} = (\mathcal{D}_x, d_y), \quad \nabla_{(\delta,D)} = (\delta_x, D_y)^T. \tag{3.22}$$

The discrete Laplacian operator $\Delta_h: \mathcal{E}^{ew}_{x \times \bar{y}} \cup \mathcal{E}^{ns}_{\bar{x} \times y} \to \mathcal{E}^{ew}_{x \times y} \cup \mathcal{E}^{ns}_{x \times y}$ for the variable **u** is defined as

$$\Delta_h \mathbf{u} = \left(\nabla_{(D,\delta)} \cdot (\nabla_{(d,\mathcal{D})} u), \nabla_{(\delta,D)} \cdot (\nabla_{(\mathcal{D},d)} v)\right)^T. \tag{3.23}$$

Throughout this paper, we denote the cell-centered, edge-centered, and vertex-centered discrete functions as follows:

cell centered functions:
$$\phi$$
, ψ , ϕ_0 , p , μ , $\in \mathcal{C}_{x \times y} \cup \mathcal{C}_{\bar{x} \times y} \cup \mathcal{C}_{x \times \bar{y}} \cup \mathcal{C}_{\bar{x} \times \bar{y}}$, (3.24)

east west edge centered functions:
$$u, r \in \mathcal{E}_{x \times y}^{ew} \cup \mathcal{E}_{x \times \bar{y}}^{ew}$$
 (3.25)

north south edge centered functions:
$$v, w \in \mathcal{E}^{ns}_{x \times y} \cup \mathcal{E}^{ew}_{\bar{x} \times y}$$
 (3.26)

vertex centered functions:
$$f, g \in \mathcal{V}_{x \times y}^{vc}$$
. (3.27)

Define the edge-to-center average and difference operator as $a_x, d_x : \mathcal{E}^{ew}_{x \times \bar{y}} \to \mathcal{C}_{x \times \bar{y}}$ and $a_y, d_y : \mathcal{E}^{ew}_{\bar{x} \times y} \to \mathcal{C}_{\bar{x} \times y}$ in component-wise via

$$a_{x}u_{i,j} = \frac{1}{2}(u_{i+\frac{1}{2},j} + u_{i-\frac{1}{2},j}), \quad d_{x}u_{i,j} = \frac{1}{h_{x}}(u_{i+\frac{1}{2},j} - u_{i-\frac{1}{2},j}), \tag{3.28}$$

$$a_y v_{i,j} = \frac{1}{2} (v_{i,j+\frac{1}{2}} + v_{i,j-\frac{1}{2}}), \quad d_y v_{i,j} = \frac{1}{h_y} (v_{i,j+\frac{1}{2}} - v_{i,j-\frac{1}{2},j}).$$
 (3.29)

The center to edge average and difference operators as $A_x, D_x: \mathcal{C}_{\bar{x} \times \bar{y}} \to \mathcal{E}^{ew}_{x \times \bar{y}}$ and $A_y, D_y: \mathcal{C}_{\bar{x} \times \bar{y}} \to \mathcal{E}^{ew}_{x \times y}$ in component-wise by

$$A_{x}\phi_{i+\frac{1}{2},j} = \frac{1}{2}(\phi_{i+1,j} + \phi_{i,j}), \quad D_{x}\phi_{i+\frac{1}{2},j} = \frac{1}{h_{x}}(\phi_{i+1,j} - \phi_{i,j}), \tag{3.30}$$

$$A_{y}\phi_{i,j+\frac{1}{2}} = \frac{1}{2}(\phi_{i,j+1} + \phi_{i,j}), \quad D_{y}\phi_{i,j+\frac{1}{2}} = \frac{1}{h_{x}}(\phi_{i,j+1} - \phi_{i,j}). \tag{3.31}$$

The vertex to edge average and difference operators are defined as $\mathfrak{a}_x, \delta_x : \mathcal{V}^{vc}_{x \times y} \to \mathcal{E}^{ns}_{x \times y}$ and $\mathfrak{a}_y, \delta_y : \mathcal{V}^{vc}_{x \times y} \to \mathcal{E}^{ew}_{x \times y}$ in component-wise forms

$$a_{x}f_{i,j+\frac{1}{2}} = \frac{1}{2} (f_{i+\frac{1}{2},j+\frac{1}{2}} + f_{i-\frac{1}{2},j+\frac{1}{2}}), \quad \delta_{x}f_{i,j+\frac{1}{2}} = \frac{1}{h_{x}} (f_{i+\frac{1}{2},j} - f_{i-\frac{1}{2},j}), \tag{3.32}$$

$$a_{y}g_{i+\frac{1}{2},j} = \frac{1}{2}(g_{i+\frac{1}{2},j+\frac{1}{2}} + g_{i+\frac{1}{2},j-\frac{1}{2}}), \quad \delta_{y}g_{i+\frac{1}{2},j} = \frac{1}{h_{y}}(g_{i+\frac{1}{2},j+\frac{1}{2}} - g_{i+\frac{1}{2},j-\frac{1}{2}}). \tag{3.33}$$

The edge to vertex average and difference operators $\mathcal{A}_x, \mathcal{D}_x : \mathcal{E}^{ns}_{\bar{x} \times y} \to \mathcal{V}^{vc}_{x \times y}$ and $\mathcal{A}_y, \mathcal{D}_y : \mathcal{E}^{ew}_{x \times \bar{y}} \to \mathcal{V}^{vc}_{x \times y}$ are defined as

$$\mathcal{A}_{x}v_{i+\frac{1}{2},j+\frac{1}{2}} = \frac{1}{2}(v_{i+1,j+\frac{1}{2}} + v_{i,j+\frac{1}{2}}), \quad \mathcal{D}_{x}v_{i+\frac{1}{2},j+\frac{1}{2}} = \frac{1}{h_{x}}(v_{i+1,j+\frac{1}{2}} - v_{i,j+\frac{1}{2}}), \quad (3.34)$$

$$\mathcal{A}_{y}u_{i+\frac{1}{2},j+\frac{1}{2}} = \frac{1}{2}(u_{i+\frac{1}{2},j+1} + u_{i+\frac{1}{2},j}), \quad \mathcal{D}_{y}u_{i+\frac{1}{2},j+\frac{1}{2}} = \frac{1}{h_{y}}(u_{i+\frac{1}{2},j+1} - u_{i+\frac{1}{2},j}). \tag{3.35}$$

We define the vertex to cell-center operator as $A: \mathcal{V}_{x\times}^{vc} \to \mathcal{C}_{x\times y}$

$$Af_{i,j} = \frac{1}{4} \left(f_{i+\frac{1}{2},j+\frac{1}{2}} + f_{i-\frac{1}{2},j+\frac{1}{2}} + f_{i+\frac{1}{2},j-\frac{1}{2}} + f_{i-\frac{1}{2},j-\frac{1}{2}} \right). \tag{3.36}$$

Based on the above definitions, we define the following discrete 2D weighted inner-products

$$(\phi,\psi)_2 = h_x h_y \sum_{i=1}^{N_x} \sum_{j=1}^{N_y} \phi_{i,j} \psi_{i,j}, \quad [u,r]_{ew} = (a_x(ur),1)_2, \tag{3.37}$$

$$[v,w]_{ns} = (a_v(vw),1)_2, \quad \langle f,g \rangle_{vc} = (A(fg),1)_2,$$
 (3.38)

and the corresponding discrete norms,

$$\|\phi\|_2 = \sqrt{(\phi,\phi)_2}, \quad \|u\|_{ew} = \sqrt{[u,u]_{ew}}, \quad \|v\|_{ns} = \sqrt{[v,v]_{ns}}, \quad \|f\|_{vc} = \sqrt{\langle f,f \rangle_{vc}}.$$
 (3.39)

For the edge-centered velocity $\mathbf{u} = (u, v)^T$, $u \in_{x \times \bar{y}}^{evv}$, $v \in \mathcal{E}_{\bar{x} \times y}^{ns}$, we defined the norms as follows

$$\|\nabla_h \mathbf{u}\|_2 = \sqrt{\|d_x u\|_2^2 + \|\mathcal{D}_y u\|_{vc}^2 + \|\mathcal{D}_x v\|_{vc}^2 + \|d_y v\|_2^2}.$$
 (3.40)

We also define the discretized volume

$$V_h(\phi) = h_x h_y \sum_{i=1}^{N_x} \sum_{j=1}^{N_y} (1 - \phi_{0,ij}) h(\phi_{ij}). \tag{3.41}$$

With the notations above, the fully-discrete scheme for the SSVM-BDF2 scheme (3.3a)-(3.3g) is achieved as follows.

Scheme 3.2 (fully-discrete SSVM-BDF2 scheme). Let $\delta t > 0$ denote the time step and the grid function $\mathbf{u}^{n-1} = (u^{n-1}, v^{n-1})^T \in \mathcal{E}^{ew}_{x \times y} \times \mathcal{E}^{ns}_{x \times y}, \phi^{n-1} \in \mathcal{C}_{x \times y} \text{ and } \mathbf{u}^n = (u^n, v^n)^T \in \mathcal{E}^{ew}_{x \times y} \times \mathcal{E}^{ns}_{x \times y}, \phi^n \in \mathcal{C}_{x \times y}$ be the solution at t_{n-1} and t_n , respectively, we are ready to find $\mathbf{u}^{n+1} = (u^{n+1}, v^{n+1})^T \in \mathcal{E}^{ew}_{x \times y} \times \mathcal{E}^{ns}_{x \times y}$ and $\phi^{n+1} \in \mathcal{C}_{x \times y}$ at t_{n+1} , such that

$$\min_{\alpha_i^{n+1}} \omega_1 |\alpha_1^{n+1}|^2 + \omega_2 |\alpha_2^{n+1}|^2, \tag{3.42a}$$

s.t.
$$\frac{a\phi^{n+1} - b\phi^n + c\phi^{n-1}}{2\delta t} + \nabla_d \cdot \left((\mathbf{A}\phi_*^{n+1})\mathbf{u}_*^{n+1} \right) = -M(1 - \phi_0)\mu[\phi^{n+1}, \phi_*^{n+1}] + \alpha_1^{n+1}h[\mathbf{u}_*^{n+1}, \phi_*^{n+1}],$$
(3.42b)

$$\mu[\phi^{n+1},\phi_*^{n+1}] = -\gamma_1 \nabla_d \cdot \left((\mathbf{A}(1-\phi_0)) \nabla_D \phi^{n+1} \right) + f'(\phi_*^{n+1}) + \gamma_3 g'(\phi_*^{n+1}) |\nabla_d (\mathbf{A}\phi_0)| \cos\theta + \sigma(1-\phi_0) h'(\phi_*^{n+1}) \left(V_h(\phi_*^{n+1}) - V_0 \right) + S(\phi^{n+1} - \phi_*^{n+1}),$$
(3.42c)

$$\rho\left(\frac{a\widetilde{\mathbf{u}}^{n+1} - b\mathbf{u}^n + c\mathbf{u}^{n-1}}{2\delta t} + B_h(\mathbf{u}_*^{n+1}, \mathbf{u}_*^{n+1})\right) = -\nabla_D p^n + \eta \Delta_h \widetilde{\mathbf{u}}^{n+1} - \mathbf{A}\phi_*^{n+1} \nabla_D \mu_*^{n+1} + \alpha_2^{n+1} \mathbf{g}[\mathbf{u}_*^{n+1}],$$
(3.42d)

$$\rho \frac{a(\mathbf{u}^{n+1} - \widetilde{\mathbf{u}}^{n+1})}{2\delta t} = -\nabla_D(p^{n+1} - p^n), \tag{3.42e}$$

$$\nabla_d \cdot \mathbf{u}^{n+1} = 0, \tag{3.42f}$$

$$\frac{a\mathcal{E}^{n+1} - b\mathcal{E}^n + c\mathcal{E}^{n-1}}{2\delta t} = -\eta \|\nabla_h \mathbf{u}_*^{n+1}\|_2^2 - \left\|\sqrt{M(1-\phi_0)}\mu_*^{n+1}\right\|_2^2,\tag{3.42g}$$

where $\mathbf{u}_*^{n+1} = (u_*^{n+1}, v_*^{n+1})^T$ and ϕ_*^{n+1} are pre-computed by solving (3.1a)-(3.1e), and

$$B_{h}(\mathbf{u}_{*}^{n+1},\mathbf{u}_{*}^{n+1}) = \frac{1}{2} \begin{pmatrix} u_{*}^{n+1}D_{x}(a_{x}u_{*}^{n+1}) + A_{x}(d_{x}(u_{*}^{n+1})^{2}) + \mathfrak{a}_{y}(\mathcal{A}_{x}v_{*}^{n+1}\mathcal{D}_{y}u_{*}^{n+1}) + \delta_{y}(\mathcal{A}_{y}u_{*}^{n+1}\mathcal{A}_{x}v_{*}^{n+1}) \\ \mathfrak{a}_{x}(\mathcal{A}_{y}u_{*}^{n+1}\mathcal{D}_{x}v_{*}^{n+1}) + \delta_{x}(\mathcal{A}_{y}u_{*}^{n+1}\mathcal{A}_{x}v_{*}^{n+1}) + v_{*}^{n+1}D_{y}(a_{y}v_{*}^{n+1}) + A_{y}(d_{y}(v_{*}^{n+1})^{2}) \end{pmatrix}.$$

Remark 3.7. The fully-discrete scheme (3.42a)-(3.42f) is developed by using finite difference approximation that admits the summation-by-parts with adiabatic boundary conditions (3.4) on a staggered grid and energy stable. Here we leave the proof details for the interested readers, as the derivations are similar to the proof of the Theorem 3.1.

3.3 Efficient Implementation processes of the fully-discrete SSVM-BDF2 scheme

We close this section by recapping a brief illustration of the practical implementation of the proposed scheme (3.42a)-(3.42f). In the first step, we now discuss the detailed implementation of the solutions (ϕ_*^{n+1} , \mathbf{u}_*^{n+1}). By some simple calculations, the scheme (3.1a) and (3.1b) at the fully-discrete level can be written as

$$A_h(\phi_0)\phi_*^{n+1} = H_h(\phi^{n-1}, \phi^n, \overline{\phi}^{n+1}, \overline{\mathbf{u}}^{n+1}), \tag{3.43}$$

where the coefficient matrix of $A_h(\phi_0)$ depends on ϕ_0 , that is,

$$A_h(\phi_0)(\bullet) = \frac{a}{2\delta t}(\bullet) + M(1 - \phi_0) \left(-\gamma_1 \nabla_d \cdot (\mathbf{A}(1 - \phi_0) \nabla_D(\bullet)) + S(\bullet) \right), \tag{3.44}$$

and the right-hand term $H_h(\phi^{n-1},\phi^n,\overline{\phi}^{n+1},\overline{\mathbf{u}}^{n+1})$ is given by

$$H_{h}(\phi^{n-1},\phi^{n},\overline{\phi}^{n+1},\overline{\mathbf{u}}^{n+1}) = \frac{b\phi^{n} - c\phi^{n-1}}{2\delta t} - \nabla_{d} \cdot \left((\mathbf{A}\overline{\phi}^{n+1})\overline{\mathbf{u}}^{n+1} \right) - M(1-\phi_{0}) \left[f'(\overline{\phi}^{n+1}) + \gamma_{3}g'(\overline{\phi}^{n+1}) |\nabla_{d}(\mathbf{A}\phi_{0})| \cos\theta + \sigma(1-\phi_{0})h'(\overline{\phi}^{n+1}) \left(V_{h}(\overline{\phi}^{n+1}) - V_{0} \right) - S\overline{\phi}^{n+1} \right].$$

$$(3.45)$$

Although the coefficient matrix $A_h(\phi_0)$ is not constant, it is time-independent and can be calculated in advance. Therefore, the system (3.43) can be efficiently solved by a preconditioned conjugate gradient iteration with a constant coefficient problem as the preconditioner that does not require explicitly building the matrix. Indeed, it only needs a subroutine to compute the matrix-vector product.

It follows from (3.1c)-(3.1e) in the fully-discrete level that

$$D_h \widetilde{\mathbf{u}}_*^{n+1} = G_h(\mathbf{u}^{n-1}, \mathbf{u}^n, \overline{\mathbf{u}}^{n+1}), \tag{3.46}$$

$$\rho \frac{a(\mathbf{u}_{*}^{n+1} - \widetilde{\mathbf{u}}_{*}^{n+1})}{2\delta t} = -\nabla_{D}(p^{n+1} - p^{n}), \tag{3.47}$$

$$\nabla_d \cdot \mathbf{u}_*^{n+1} = 0, \tag{3.48}$$

where $D_h(\bullet) = \frac{a\rho}{2\delta t}(\bullet) - \eta \Delta_h(\bullet)$ and

$$G_{h}(\mathbf{u}^{n-1},\mathbf{u}^{n},\overline{\mathbf{u}}^{n+1}) = \frac{\rho(b\mathbf{u}^{n} - c\mathbf{u}^{n-1})}{2\delta t} - \rho B_{h}(\overline{\mathbf{u}}^{n+1},\overline{\mathbf{u}}^{n+1}) - (\mathbf{A}\phi_{*}^{n+1})\nabla_{D}\mu[\overline{\mu}^{n+1},\overline{\mu}^{n+1}] - \nabla_{D}p^{n}.$$

$$(3.49)$$

Since $G_h(\mathbf{u}^{n-1},\mathbf{u}^n,\overline{\mathbf{u}}^{n+1})$ includes all explicit terms in (3.49), then $\widetilde{\mathbf{u}}_*^{n+1}$ can be efficiently computed by solving a linear algebraic system that involves a constant and time-independent coefficient matrix D_h . This matrix can also be pre-computed, thereby reducing the computational cost. It it noticing that p^{n+1} can be firstly computed by using incompressible condition $\nabla_d \cdot \mathbf{u}_*^{n+1} = 0$ and then \mathbf{u}_*^{n+1} is updated via the equation (3.47). In a word, the velocity-field \mathbf{u}_*^{n+1} and phase filed ϕ_*^{n+1} are totally linear and decoupled. This means very efficient practical calculations.

In the second step, we rewrite the scheme (3.42b)-(3.42f) in an equivalent form as follows

$$A_h(\phi_0)\phi^{n+1} = H_h(\phi^{n-1}, \phi^n, \phi_*^{n+1}, \mathbf{u}_*^{n+1}) + \alpha_1^{n+1}h[\mathbf{u}_*^{n+1}, \phi_*^{n+1}], \tag{3.50}$$

$$D_h \widetilde{\mathbf{u}}^{n+1} = G_h(\mathbf{u}^{n-1}, \mathbf{u}^n, \mathbf{u}_*^{n+1}) + \alpha_2^{n+1} \mathbf{g}[\mathbf{u}_*^{n+1}], \tag{3.51}$$

$$\rho \frac{a(\mathbf{u}^{n+1} - \widetilde{\mathbf{u}}^{n+1})}{2\delta t} = -\nabla_D(p^{n+1} - p^n), \tag{3.52}$$

$$\nabla_d \cdot \mathbf{u}^{n+1} = 0. \tag{3.53}$$

Further, one can express the solutions ϕ^{n+1} and $\tilde{\mathbf{u}}^{n+1}$ of the system (3.50) and (3.51) in the following forms

$$\phi^{n+1} = \hat{\phi}^{n+1} + \alpha_1^{n+1} \hat{h}^{n+1}, \tag{3.54}$$

$$\tilde{\mathbf{u}}^{n+1} = \hat{\mathbf{u}}^{n+1} + \alpha_2^{n+1} \hat{\mathbf{g}}^{n+1},$$
 (3.55)

where $\hat{\phi}^{n+1}$, \hat{h}^{n+1} , $\hat{\mathbf{u}}^{n+1}$ and $\hat{\mathbf{g}}^{n+1}$ satisfy the following four linear system

$$\{\hat{\phi}^{n+1}, \hat{h}^{n+1}\} = A_h^{-1}(\phi_0) \left\{ H_h(\phi^{n-1}, \phi^n, \phi_*^{n+1}, \mathbf{u}_*^{n+1}), h[\mathbf{u}_*^{n+1}, \phi_*^{n+1}] \right\}, \tag{3.56}$$

$$\{\hat{\mathbf{u}}^{n+1}, \hat{\mathbf{g}}^{n+1}\} = D_h^{-1} \left\{ G_h(\mathbf{u}^{n-1}, \mathbf{u}^n, \mathbf{u}_*^{n+1}), \mathbf{g}[\mathbf{u}_*^{n+1}] \right\}, \tag{3.57}$$

where A_h^{-1} and D_h^{-1} denote the inverse matrix of A_h and D_h , respectively. It is easy to solve the above system since they are linear, decoupled, and all the right-hand terms are known. Then plugging (3.54)-(3.55) into (3.42g) yields the following scalar nonlinear algebraic equation

$$N(\alpha_{1}^{n+1},\alpha_{2}^{n+1}) = a\mathcal{E}[\hat{\boldsymbol{\phi}}^{n+1} + \alpha_{1}^{n+1}\hat{\boldsymbol{h}}^{n+1},\hat{\mathbf{u}}^{n+1} - \nabla_{D}(\nabla_{d}\cdot\nabla_{D})^{-1}\nabla_{d}\cdot\hat{\mathbf{u}}^{n+1} + \alpha_{2}^{n+1}\hat{\mathbf{g}}^{n+1}] - b\mathcal{E}^{n} + c\mathcal{E}^{n-1} + 2\delta t\eta \|\nabla_{h}\mathbf{u}_{*}^{n+1}\|_{2}^{2} + 2\delta t \|\sqrt{M(1-\phi_{0})}\mu_{*}^{n+1}\|_{2}^{2} = 0.$$
(3.58)

It remains to determine the supplementary variables $(\alpha_1^{n+1}, \alpha_2^{n+1})$. Once these variables are known, the field unknowns $(\phi^{n+1}, \mathbf{u}^{n+1})$ can be updated directly by utilizing (3.54)-(3.55).

Finally, with the aid of the SVM formulation, the proposed numerical scheme from (3.42a)-(3.42g) can be transformed into a constrained minimization problem as follows

$$\min_{\alpha_i^{n+1}} \omega_1 |\alpha_1^{n+1}|^2 + \omega_2 |\alpha_2^{n+1}|^2, \tag{3.59}$$

s.t.
$$N(\alpha_1^{n+1}, \alpha_2^{n+1}) = 0.$$
 (3.60)

To solve it, we consider the augmented Lagrangian function by introducing a Lagrange multiplier λ and a penalty parameter κ , which is expressed as follows

$$\mathcal{L}_{\kappa}(\alpha_{1}^{n+1},\alpha_{2}^{n+1},\lambda) = \omega_{1}|\alpha_{1}^{n+1}|^{2} + \omega_{2}|\alpha_{2}^{n+1}|^{2} + \lambda N(\alpha_{1}^{n+1},\alpha_{2}^{n+1}) + \frac{\kappa}{2}N^{2}(\alpha_{1}^{n+1},\alpha_{2}^{n+1}). \tag{3.61}$$

Applying the augmented Lagrangian method to this problem yields

$$\alpha^{n+1,(k+1)} = \min_{\alpha_i} \mathcal{L}_{\kappa}(\alpha_1^{n+1}, \alpha_2^{n+1}, \lambda^{(k)}), \quad i = 1, 2,$$
(3.62)

$$\lambda^{(k+1)} = \lambda^{(k)} + \kappa N(\alpha_1^{n+1,(k+1)}, \alpha_2^{n+1,(k+1)}). \tag{3.63}$$

where $\alpha^{n+1} = (\alpha_1^{n+1}, \alpha_2^{n+1})^T$ and the index $k = 0, 1, 2, \cdots$ denotes the iteration step. Here the augmented Lagrangian is minimized jointly with respect to the two primal variables α_1 and α_2 . Now, combining all the above treatments for solving α_1^{n+1} and α_2^{n+1} , we elaborate the detailed solution procedures as follows.

Algorithm 1 Solving problem (3.59) and (3.60) by augmented Lagrangian method.

Input: Initialize $\alpha_1^{n+1,(0)}$ and $\alpha_2^{n+1,(0)}$, the multiplier $\lambda^{(0)}$ and the updated constant of penalty factor $\kappa^{(0)}$. Set the iterative tolerance ϵ .

Solve:
$$\alpha^{(k+1)} = (\alpha_1^{n+1,(k+1)}, \alpha_2^{n+1,(k+1)})^T = \min_{\alpha_i} \mathcal{L}_{\kappa}(\alpha_1^{n+1}, \alpha_2^{n+1}, \lambda^{(k)}).$$

if:
$$|N(\boldsymbol{\alpha}^{n+1,(k+1)})| < \epsilon$$
 then

return the approximation solution $\alpha^{n+1,(k+1)}$ and $\lambda^{(k)}$, and then stop the iteration.

end if

Update the multiplier: $\lambda^{(k+1)} = \lambda^{(k)} + \kappa^{(k)} N(\alpha_1^{n+1,(k+1)}, \alpha_2^{n+1,(k+1)})$.

Update the penalty factor: $\kappa^{(k+1)} = \varrho \kappa^{(k)}$.

We must avoid the constant penalty factor growing too fast or too slow. An empirical selection is $\varrho \in [2,10]$, such that the sequence $\alpha^{n+1,(k)}$ can converge quickly. Ample numerical tests in this paper also support our claim the supplementary variables $(\alpha_1^{n+1}, \alpha_2^{n+1})$ is determined very accurately and efficiently by the above Algorithm 1 so that the cost is negligible.

Remark 3.8. It is noticeable that for the SSVM-BDF2 scheme, two sets of field variables for each velocity $\bf u$ and phase-field variable ϕ are computed and decoupled, together with a nonlinear scalar equation. Within each step, our proposed scheme allows for more straightforward calculations for the PF-FSI-MCL model by solving a few decoupled Helmholtz or Poisson-type systems with a constant pre-computable coefficient matrix, remarkably improving computing efficiency. Although the scheme requires the solution of a scalar nonlinear equation, the cost for solving the scalar nonlinear system is relatively cheap and efficient using the augmented Lagrangian approach compared to the total computation cost.

Remark 3.9. In general, many options for artificial functions can be manually assigned to obtain the perturbed system. How to choose them to make the extended system more accessible, more efficient to solve, or the solution more accurate would be an interesting and open question to explore further.

Remark 3.10. We emphasize that the obtained real-valued $(\alpha_1^{n+1}, \alpha_2^{n+1}, \lambda)$ may not be the exact solution of the equation in (3.59)-(3.60), but the numerical solution approximates the exact one very accurately. In this sense, the discrete energy dissipative relation (3.42f) can be warranted in the round-off of the machine, which implies our proposed SSVM-BDF2 scheme satisfies the energy stable via Theorem 3.1.

Remark 3.11. This model is highly coupled, and the numerical scheme involves a scalar non-linearity problem. However, we never observe any problems with the existence and uniqueness of the solution in all our extensive numerical experiments. Furthermore, although we only study the proof of the original energy dissipation law, determining how to achieve optimal error estimates for this scheme also brings enormous challenges and opportunities. In the literature, several results on the convergence analysis for the phase-field hydrodynamics models exist [6,8–10,18,43]. We plan to address the issue in our future research.

4 Numerical results

In this section, we first present the numerical convergence test of the proposed SSVM-BDF2 scheme. We then report several numerical tests in a complex region to confirm the developed model's capability and the proposed scheme's efficiency. For simplicity, we choose $\rho=1$ and $\omega_1=\omega_2=1$ in the rest of this section. Unless otherwise specified, the numerical simulations are performed in the computational domain $\Omega=[0,L_x]\times[0,L_y]$ with $L_x=1$ and $L_y=1$. We use 256×256 spatial meshes, and the parameters are set as $\eta=1$, S=10, $\epsilon=0.0019$, $\gamma_1=\epsilon^2$, $\gamma_2=0.25$ and $\gamma_3=\epsilon/12\sqrt{2}$. Additionally, for simplicity of notations, we summarized some initial profiles in later discussions in Figure 1. The initial profiles for benchmarking contact angles are provided in Figure 1 (a)-(b), and the initial profile for benchmarking the rounding dynamics without or with flows are provided in Figure 1 (c)-(d). For more detailed information about these benchmark problems, please refer to [30,42,50] and the references therein.

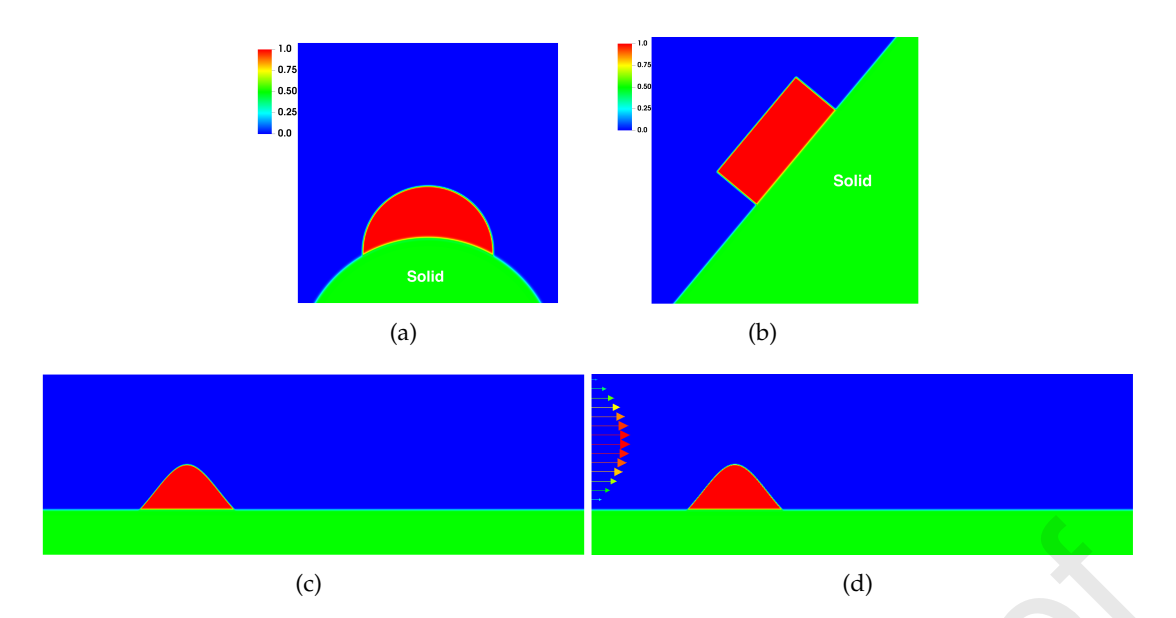


Figure 1: The initial profiles. (a)-(b) the initial profiles of the contact angles; (c)-(d) The initial profiles of rounding dynamics, with (c) without inflow, and (d) with inflow.

Example 4.1 (Mesh refinement test). In this example, we conduct a convergence test by considering the Cauchy sequence to measure the proposed numerical scheme as second-order in time and space. We compute the PF-FSI-MCL model with the initial condition for the phase variable $\phi(x,y,0) = \frac{1}{2} + \frac{1}{2}\cos(2\pi x)\cos(2\pi y)$, and the initial velocity field is set to zero. Some model parameters are given by $M=10^{-4}$, $\epsilon=0.01$, $\sigma=100$, $\theta=45^{\circ}$, and $\phi_0=\phi(x,y,0)$. The homogeneous Neumann boundary conditions for ϕ, μ, p, ϕ_0 , and the velocity field **u** are applied on the homogeneous Dirichlet boundary. We simultaneously refine the time and space meshes with N = 16,32,64,128,256 and $\delta t = 1/32,1/64,1/128,1/256,1/512$. Here, we choose the number of the spatial grids as $N_x = N_y = N$. The errors are calculated as the difference between the solutions on the coarse mesh and that on the adjacent finer mesh at the position of the coarser mesh. In Table 1 and Table 2, we display the discrete L^2 and L^{∞} errors for the velocity field $\mathbf{u} = (u,v)^T$ and phase-field variable ϕ at the final time T=1. Recall the norm for the vector field $\|\mathbf{u}\|_2 = \sqrt{\|u\|_{ew}^2 + \|v\|_{ns}^2}$, and $\|\mathbf{u}\|_{\infty} = \max\{|u_{ij}|, |v_{ij}|\}$; the norm for the scalar field $\|\phi\|_2 = \sqrt{(\phi,\phi)_2}$ and $\|\phi\|_{\infty} = \max |\phi_{ii}|$. From Table 1 and Table 2, we observe the convergence rate of the numerical errors can reach approximately second-order accuracy for all variables. This indicates that the developed SSVM-BDF2 scheme is second-order in time and space.

Table 1: Mesh refinement test of the SSVM-BDF2 scheme for velocity field ${\bf u}$.

δt	N	Error		Order	
	-	L^2	L^{∞}	L^2	L^{∞}
$\frac{\frac{1}{32} \& \frac{1}{64}}{}$	16&32	1.465e-06	6.639e-06	_	_
$\frac{1}{64}$ & $\frac{1}{128}$	32 & 64	1.908e-07	1.972e-06	2.942	1.751
$\frac{1}{128} \& \frac{1}{256}$	64 & 128	3.427e-08	2.121e-07	2.477	3.217
$\frac{1}{256}$ & $\frac{1}{512}$		8.605e-09	5.360e-08	1.994	1.985

Table 2: Mesh refinement test of SSVM-BDF2 for phase-field variable	e
ϕ .	

δt	N	Error		Order	
	-	L^2	L^{∞}	L^2	L^{∞}
$\frac{\frac{1}{32} \& \frac{1}{64}}{}$	16&32	1.201e-03	4.621e-03	_	_
$\frac{1}{64}$ & $\frac{1}{128}$	32 & 64	3.011e-04	1.192e-03	1.996	1.954
$\frac{1}{128} \& \frac{1}{256}$	64 & 128	7.533e-05	3.004e-04	1.999	1.989
$\frac{1}{256}$ & $\frac{1}{512}$	128 & 256	1.884e-05	7.525e-05	1.999	1.997

Example 4.2 (Test the influence of stabilization and spinodal decomposition). So far, there is no theoretical way to determine the optimal value of the stabilization parameter S. Therefore, we will perform a numerical test of phase separation behavior under hydrodynamical environments in a complex domain to empirically choose appropriate values and illustrate the necessity of adding the stabilization term to our developed SSVM-BDF2 scheme. To solve the problem, we set M=10. We fix the contact angle $\theta=30^\circ$ and choose $\phi_0=0.5+0.5 \tanh(\sqrt{(x-0.48)^2+(y-0.5)^2}-0.35-0.12\cos(5\theta))$, where $\theta=\tan^{-1}((y-0.45)/(x-0.45))$. Set the initial condition as $\phi(x,y,t=0)=0.5+0.05\cdot \mathrm{rand}(-1,1)$, and $\mathbf{u}(x,y,t=0)=\mathbf{0}$.

Here, we study the numerical performances by setting S=0, S=10, and S=50, where S=0 denotes an absence of stabilization term. We plot the evolution curves of the original energy using the SSVM-BDF2 scheme with various time steps and different values of S in Figure 2. We draw the following conclusions from these tests. The proposed scheme without the stabilization term blows up for $\delta t > 1/1024$, and shows the energy decays for smaller time steps. The energy curve of SSVM-BDF2 with S=10 decays until $\delta t \leq 1/512$, while the scheme with S=50 illustrates that the energy curve provides a monotonic decrease for all selected time steps. Compared with the absence of a stabilization term, the stabilizer "stabilizes" the proposed scheme at relatively larger time steps. However, when S=50 is added to this scheme, it performs more satisfactorily than that with S=10 at larger time steps, demonstrating an appropriate stabilizer S is extremely critical to improve the stability. In short, the stabilized scheme SSVM-BDF2 overwhelmingly defeats the non-stabilized SVM-BDF2 scheme for stability.

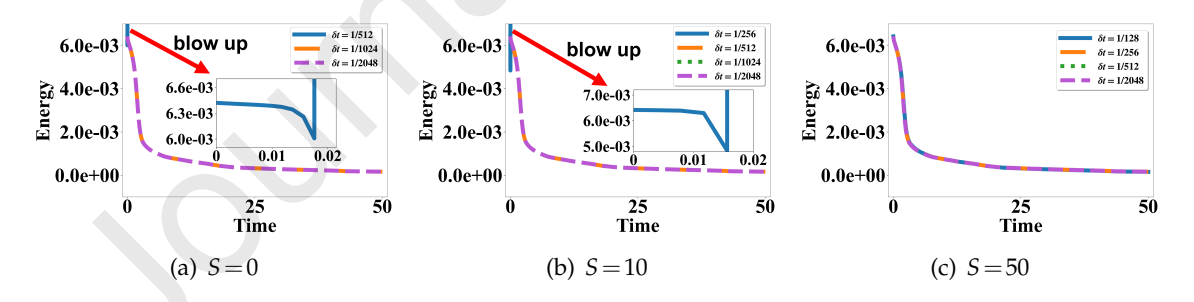


Figure 2: Time evolution of the original energy for various time steps computed by SSVM-BDF2 with different values of *S*.

We choose S=50 and $\delta t=1/256$ to conduct long simulations of coarsening dynamics on a star-shaped domain to obtain good stability and accuracy. Figure 3 visualizes the velocity fields for the coarsening dynamics with $\theta=30^\circ$ on a star-shaped domain. One can observe that the velocity field has a larger magnitude at the regions that are changing rapidly, and the effect of contact angle on the evolutional dynamics of the solid boundaries is evident.

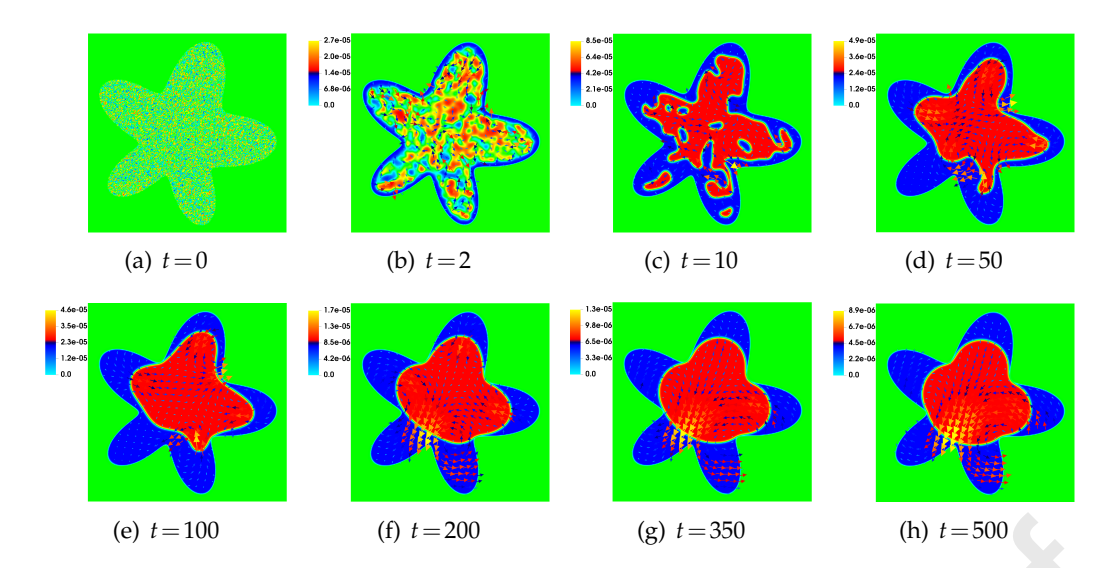


Figure 3: The visualization of the vector field for coarsening dynamics on a star-shaped domain. The snapshots are taken at t = 0, 2, 10, 50, 100, 200, 350 and 500.

Finally, the evolution of original energy, volume, and supplementary variables for coarsening dynamics are depicted in Figure 4. These numerical performances demonstrate that our developed model and scheme are very effective. One can observe that the energy decays with respect to time, the Allen-Cahn model with an additional penalty term under hydrodynamics environments indeed preserves volume, and the supplementary variables are close to zero very accurately.

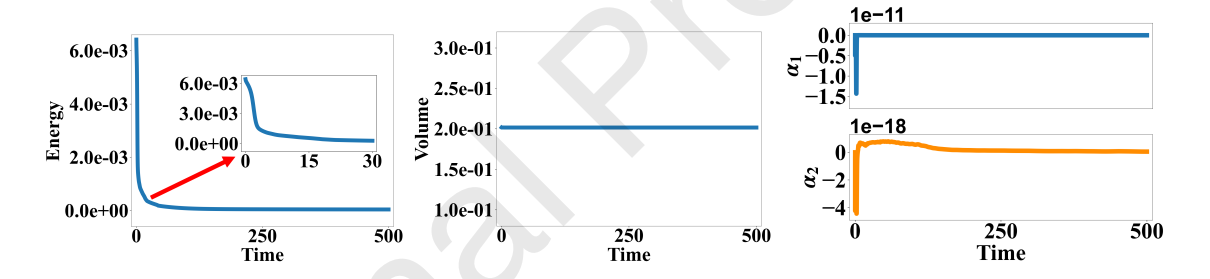


Figure 4: Time evolution of original energy, volume and supplementary variables for coarsening dynamics in Figure 3.

Example 4.3 (Impact of penalty parameter and equilibrium contact angles). In this example, we mainly study an equilibrium phase interface contacting a solid with a prescribed contact angle θ and the effect of the penalty parameter. We take the parameters as M=100. The initial velocity is set as zero, and the initial condition for the phase field variable ϕ read as

$$\phi(x,y,0) = \begin{cases} 1 - \phi_0(x,y), & \text{if } \phi_0(x,y) + \psi(x,y) > 1, \\ \psi(x,y), & \text{otherwise,} \end{cases}$$

$$(4.1)$$

where
$$\phi_0(x,y)$$
 and $\psi(x,y)$ are given by $\phi_0(x,y) = 0.5 + 0.5 \tanh\left(\frac{R_0 - \sqrt{(x-x_0)^2 + (y-y_0)^2}}{2\sqrt{2}\epsilon}\right)$ with $x_0 = 0.5$, $y_0 = -0.25$ and $R_0 = 0.5$, $\psi(x,y) = 0.5 + 0.5 \tanh\left(\frac{R_1 - \sqrt{(x-x_1)^2 + (y-y_1)^2}}{\sqrt{2}\epsilon}\right)$ with $x_1 = 0.5$, $y_1 = 0.2$ and $x_1 = 0.25$. Figure 1 (a) shows the initial profile.

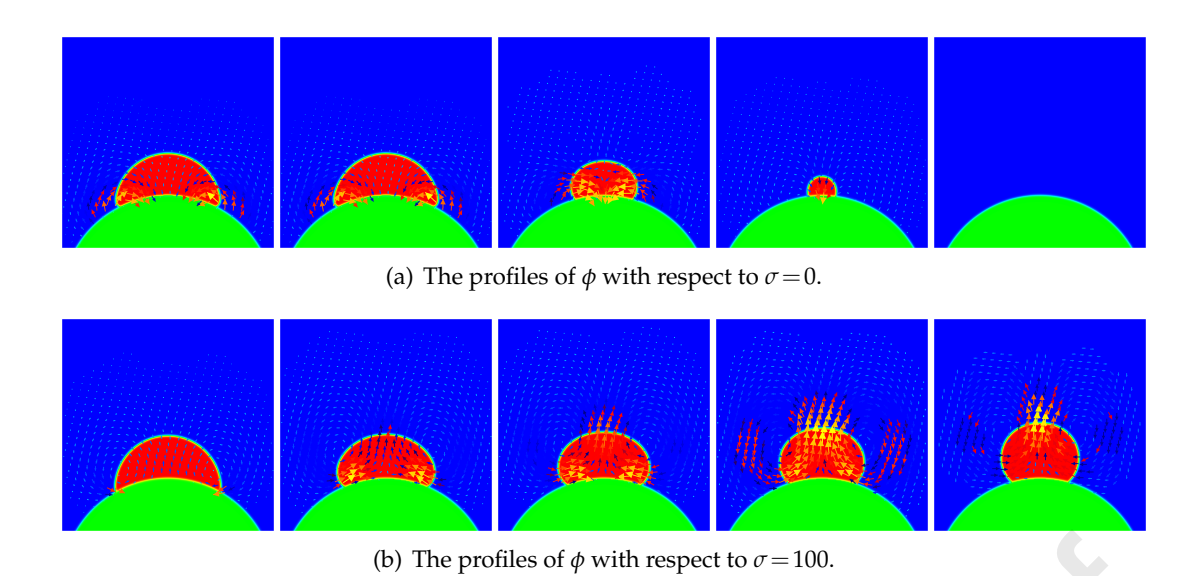


Figure 5: The visualization of the vector field and time evolution of phase interface contacting a solid boundary for different penalty parameter values σ under hydrodynamic environment. In these figures, the phase variable ϕ profiles are shown at time t=1,10,25,50 and 100.

We use time step size $\delta t=1/256$ in the implementation. The numerical results with the penalty parameter $\sigma=0$ and $\sigma=100$ are summarized in Figure 5, where the dynamics of the phase variable ϕ at various times are shown under a hydrodynamic environment and two distinct patterns of velocity field circulation can be observed. When $\sigma=0$, the profile of the droplet gradually shrinks and then disappears at the end of the simulation. Meanwhile, the velocity field consistently moves in the direction of the droplet's contraction, ultimately decreasing to zero as the one disappears. For $\sigma=100$, the final contact angle of the phase interface contacting the solid boundary is approximately equal to $\theta=60^\circ$, while the initial contact angle is set to $\theta\approx120^\circ$. The velocity field evolves under the effect of surface tension.

Meanwhile, the evolution of original energy, volume, and the supplementary variables $\alpha_1(t)$ and $\alpha_2(t)$ as functions of time with $\delta t = 1/256$ up to the final time T = 100 are summarized in Figure 6. These results indicate the proposed scheme respects the energy dissipation law. It further highlights that a large value of σ is necessary to control the volume change. The numerical results obtained for the supplementary variables are very accurate.

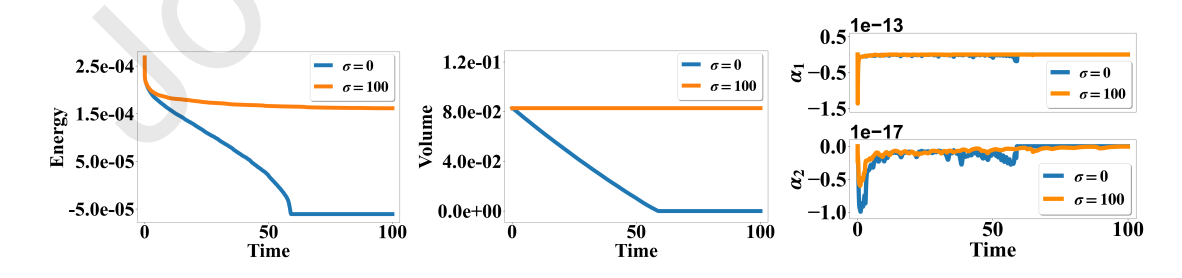
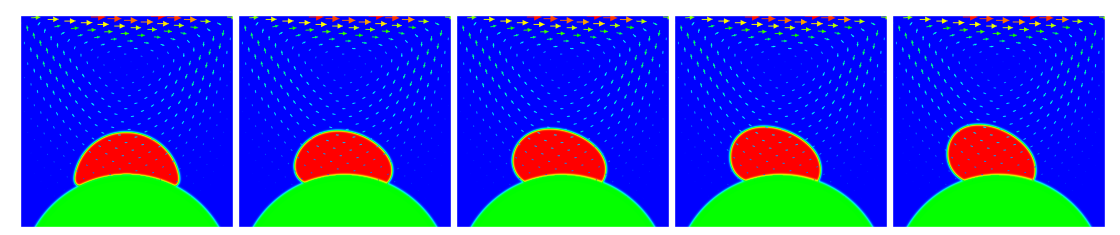
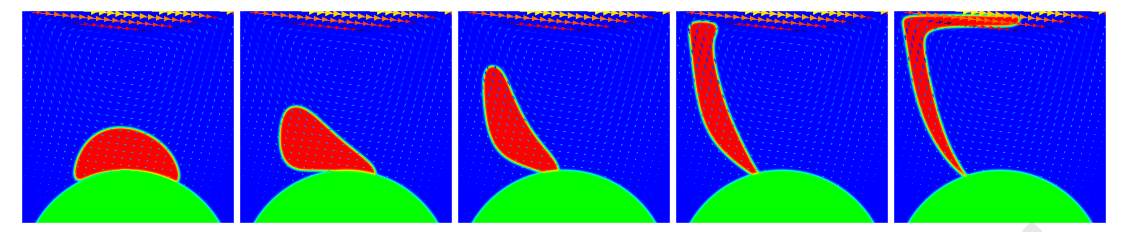


Figure 6: Time evolution of original energy, volume, and supplementary variables with respect to different penalty parameters for the dynamics of phase interface contacting a solid case in Figure 5.



(a) Weak lid-driven cavity flow with $\hat{u}_0 = 0.01$, where the snapshots are taken at t = 1,10,20,30,40.



(b) Strong lid-driven cavity flow with $\hat{u}_0 = 0.1$, where the snapshots are taken at t = 1,10,20,30,40.

Figure 7: The 2D dynamical evolution of phase interface contacting a solid boundary that is driven by two different magnitudes of the lid-driven cavity flow, where (a) the weak case with $\hat{u}_0 = 0.01$ and (b) the strong case with $\hat{u}_0 = 0.1$.

Next, we study how the lid-driven cavity flow affects the contact angle. The zero Dirichlet boundary condition for the velocity at the boundary, except at $\mathbf{u}|_{y=L_y}=(\hat{u}_0,0)^T$, where \hat{u}_0 is the magnitude of the lid-driven cavity. Similar to the previous scenario, the initial and boundary conditions for phase variable ϕ are set up accordingly. Figure 7 visualizes the dynamics of the phase variable and velocity fields for the lid-driven cavity problem with the weak and strong cases. We can observe that the drop is deformed due to the lid-driven cavity flow, and strong flow induces large deformations. Notably, the contact angle on the left of the phase interface contacting the solid boundary remains consistent with the case when there was no lid-driven cavity flow.

Finally, we perform a qualitative comparison with experimental results to showcase the effectiveness of our developed model. We set the initial conditions that are defined in (4.1) to the case of the drop impact on a solid, where $x_0 = 0.5$, $y_0 = -0.24$, $R_0 = 0.48$ and $x_1 = 0.5$, $y_1 = 0.48$ 0.26, $R_1 = 0.1$. The initial pressure is set up as in the previous scenario, except that the initial velocity reads $\mathbf{u} = (0, -1 \cdot \phi(x, y, 0))^T$. The model parameters remain at their default settings except for $\rho = 1.1$ and $\eta = 0.01$. A time step $\delta t = 10^{-3}$ and $N_x = N_y = 256$ are employed to perform this test. Figure 8 (a) shows the snapshots of the droplet impact on a solid at different times. Here, one can observe that under the action of an initial downward velocity field, the droplet undergoes noticeable deformation. Over time, the bubble eventually spreads upwards in a vertical direction. The dynamic topological changes are qualitatively similar to the experimental results [35] and the other numerical simulations [24], which are listed for comparison in Figure 8 (b) and Figure 8 (c). However, several subtle differences can be seen. On the one hand, this may be due to our lack of knowledge regarding the actual initial values. On the other hand, as highlighted in the literature [24], it is likely that the current simulation does not take into account the contact angle hysteresis and only one equilibrium contact angle is used. Overall, this result suggests that our proposed model can simulate the impact of droplets on solids.



(a) The snapshots of the drop shape during drop impact on a solid at t=0.1, 1.6, 50.



(b) Experimental results in [35].



(c) Other numerical simulations in [24].

Figure 8: (a) The 2D dynamical evolution of a droplet impact on a solid; (b) the experimental results in [35]; (c) other numerical results in [24].

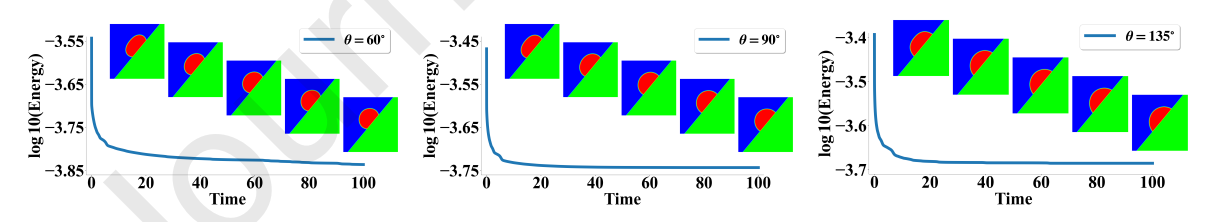
Example 4.4 (Test different contact angles). In this example, we study energy stability with different contact angles. The initial condition for the phase-field variable ϕ is given by

$$\phi(x,y,0) = \begin{cases} 1 - \phi_0(x,y), & \text{if } \phi_0(x,y) + \psi(x,y) > 1, \\ \psi(x,y), & \text{otherwise,} \end{cases}$$

$$(4.2)$$

where $\phi_0(x,y) = 0.5 + 0.5 \tanh\left(\frac{\frac{6}{5}x - y - 0.1}{2\sqrt{2}\epsilon}\right)$ and $\psi(x,y) = \begin{cases} 1, & \text{if } 0.7 < \frac{5}{6}x + y < 1.3, \frac{6}{5}x - y > -0.2, \\ 0, & \text{otherwise.} \end{cases}$

We set the initial velocity as zero, and the initial profile of ϕ is shown in Figure 1 (b).



(a) Energy evolution with $\theta = 60^{\circ}$. (b) Energy evolution with $\theta = 90^{\circ}$. (c) Energy evolution with $\theta = 135^{\circ}$.

Figure 9: The time evolution of the original energy for phase interface contacting a solid boundary with $\theta = 60^{\circ}$, 90° , 135° , where the profiles of ϕ at t = 20, 40, 60, 80, 100 are shown.

In this simulation, we adopt the SSVM-BDF2 scheme with $\delta t = 1/256$, using the same parameters as in the previous example. We vary the contact angle θ and report the corresponding energy evolutions in Figure 9. The results showcase the liquid phases evolve from the initial state to the equilibrium state, and the phase interface contacting the solid boundary closes to

the theoretical contact angle [28]. This further confirms that our proposed model and algorithm can accurately predict phase interfaces in a complex domain.

Example 4.5 (Bubble rising). In this example, we simulate the dynamics motions of one droplet under the action of gravity field on a complicated domain, which is embedded into the rectangular domain $\Omega = [0, L_x] \times [0, L_y]$ with $L_x = 1$ and $L_y = 2$. The left and right boundaries of the complicated domain are given by $l(x) = 0.01y^2\cos(5\pi y) - 0.1\sin(6\pi y) + 0.3$ and r(x) = $0.01y^2\cos(2\pi y) - 0.06\sin(6\pi y) + 0.6$, respectively. Here we still use the momentum equation (2.9) that is equipped with gravity force, that is,

$$\rho(\partial_t \mathbf{u} + \frac{1}{2}(\mathbf{u} \cdot \nabla \mathbf{u} + \nabla \cdot (\mathbf{u}\mathbf{u}))) = -\nabla p + \eta \Delta u - \phi \nabla \mu + \phi \mathbf{G}, \tag{4.3}$$

where $G = (0.9.8)^T$. The model parameters are set as $\eta = 0.1$, $\sigma = 1000$ and $\theta = 135^\circ$. To conduct this simulation, we choose $N_x = 256$, $N_y = 512$ and $\delta t = 10^{-3}$. The initial conditions for this problem read as

$$\phi(x,y,0) = 0.5 + 0.5 \tanh\left(\frac{0.1 - \sqrt{(x-0.5)^2 + (y-0.22)^2}}{\sqrt{2}\epsilon}\right),$$

$$\mathbf{u}(x,y,0) = (0,0)^T, \quad p(x,y,0) = 0.$$
(4.4)

$$\mathbf{u}(x,y,0) = (0,0)^T, \quad p(x,y,0) = 0.$$
 (4.5)

Figure 10 shows the dynamics of the rising droplet driven by gravity filed on a complicated domain. One can observe that under the influences of gravity force filed and velocity field, the initial circle droplet of the irregular domain undergoes a more considerable deformation in the rising process. For comparison, the bubble rising case on a rectangular domain is shown in Figure 11. As the initial drop profile is symmetric around the y axis and the gravity force is along the y axis, the drop should preserve axisymmetry, as observed in our numerical simulation.

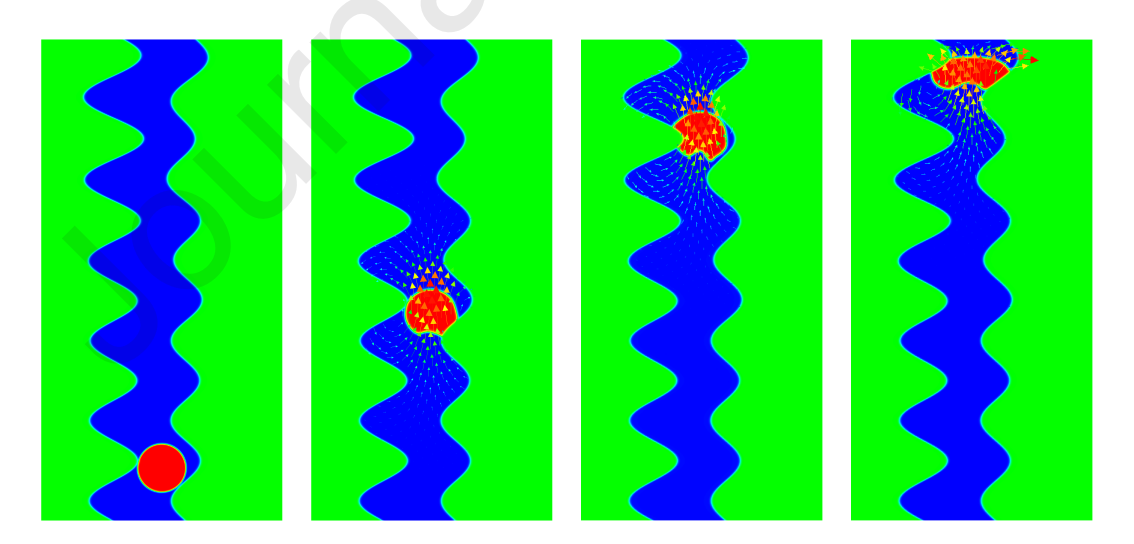


Figure 10: The dynamics of a rising droplet on a complicated domain, where the snapshots are taken at t = 0, 3, 6.3 and 8.

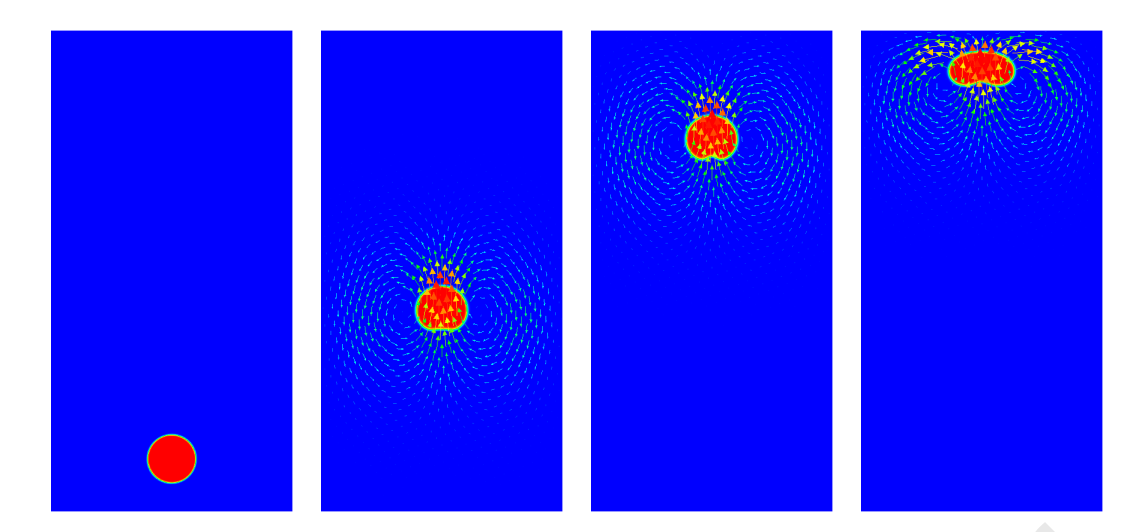


Figure 11: The dynamics of a rising droplet on a rectangular domain, where the snapshots are taken at t = 0, 3, 6.3 and 8.

In Figure 12 (a), we plot the time evolution of the energy. Under the impact of the gravity force field, the dissipation property of this system does not hold. Thus, the system may not be dissipative. The numerical results of Figure 12 (a) support the conclusion very well. From Figure 12 (b), we find that although the bubble's rising shape changes, the volume of two cases is always conserved. In Figure 12 (c), we also show the changes of supplementary variables very close to zero.

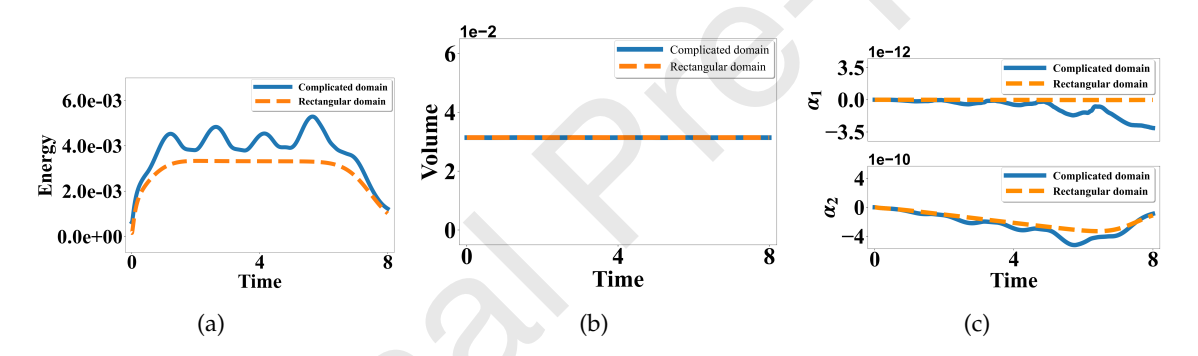


Figure 12: Time evolution of energy, volume, and supplementary variables for coarsening dynamics in Figure 10 and Figure 11.

Example 4.6 (Rounding dynamics). Lastly, we study how fluid flow affects rounding dynamics through a channel. The initial phase conditions read as follows:

$$\phi(x,y,0) = \begin{cases} 1 - \phi_0(x,y), & \text{if } \phi_0(x,y) + \psi(x,y) > 1, \\ \psi(x,y), & \text{otherwise,} \end{cases}$$

$$(4.6)$$

$$\mathbf{u}(x,y,0) = (0,0)^T, \quad p(x,y,0) = 0.$$
 (4.7)

where ϕ_0 and ψ are given by

$$\phi_0(x,y) = 0.5 + 0.5 \tanh\left(\frac{0.25 - y}{2\sqrt{2}\epsilon}\right), \ \psi(x,y,0) = 0.5 + 0.5 \tanh\left(\frac{0.5 \text{sech}(5x - 4) - y}{\sqrt{2}\epsilon}\right).$$
 (4.8)

The model parameters are set as M = 100, $\gamma_3 = \epsilon^2 / 12\sqrt{2}$, $\sigma = 1000$. We carry out numerical simulations in a 2D domain $\Omega = [0,3] \times [0,1]$ by using 768×256 spatial meshes and the time step

 δt = 1/256. We first consider how the absence of an inflow scenario affects the evolution of this rounding dynamics. Figure 1 (c) displays the initial profile without inflow. We conduct a long numerical simulation for this case by SSVM-BDF2, where the detailed evolutionary processes are shown in Figure 13. We can see that the initial profiles gradually evolve into a semi-circle shape without the phenomenon of rounding dynamics.

Further, we impose the inflow fluid on the wall boundary. The inflow velocities on upper and lower boundaries are set as zero. At the inlet, a parabolic velocity profile is adapted to the wall, i.e., $\mathbf{u}(0,y) = (0.05(1-y)(0.25-y),0)^T$ and the corresponding initial profile is shown in Figure 1 (d). In Figure 14, we plot the snapshots of the rounding dynamics with inflow at different times. One can observe that due to the influence of inflow, the triangular drop starts to scroll from left to right in the channel. During the process, its topological shape gradually becomes a circle. These numerical performances strongly support our claim that our developed model and algorithm can accurately simulate rounding dynamics.

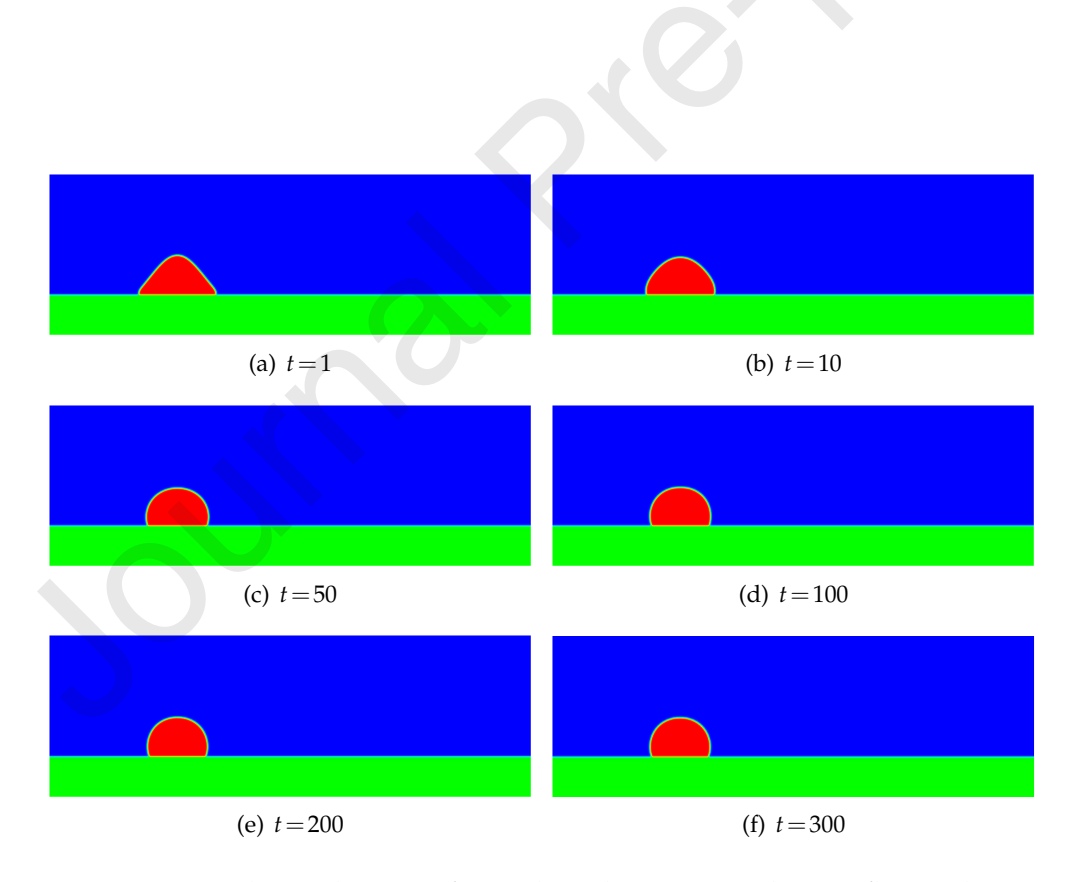


Figure 13: The evolutions of rounding dynamics without inflow. The initial condition is summarized in Figure 1(c). The profiles at time t = 1,10,50,100,200,300 are shown.

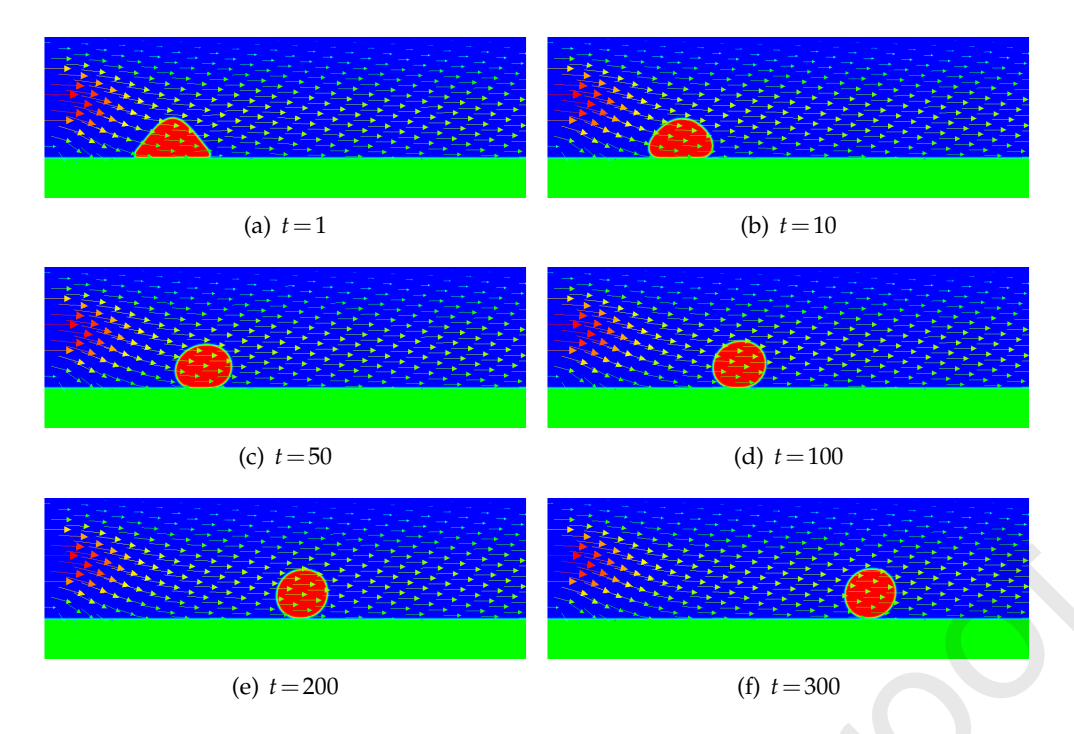


Figure 14: The evolutions of rounding dynamics with inflow. The phase field and velocity profiles at time t = 1,10,50,100,200,300 are shown, with the initial profile given in Figure 1 (d).

5 Conclusions

In this work, we proposed a new computational modeling approach to investigate the fluid-structure interaction with moving contact lines in an arbitrarily complex domain. Our proposed models couple the hydrodynamics and phase field variables through an energy variational procedure, leading to a thermodynamically consistent PDE system that respects the thermodynamic laws. The fluid-structure interaction is modeled by introducing a phase variable representing the volume fraction of one fluid and an extra auxiliary phase field variable that is time-independent to label the volume fraction of the solid structure. The system's total energy consists of the kinetic energy of the fluid mixture and free energies of the fluid-fluid and fluid-solid interactions. Additionally, a second-order Allen-Cahn equation can describe the phase field dynamics, which is easier to compute numerically than the fourth-order Cahn-Hilliard system. To circumvent a drawback of the Allen-Cahn model, we also introduce an additional penalty term in the free energy to enforce volume conservation. The numerical tests also demonstrate our developed model is valid.

Combining the supplementary variable method and the projection approach and by utilizing the implicit-explicit BDF2 scheme for temporal discretization and the second-order finite difference approach on the staggered grid for spatial discretization, we came up with a totally decoupled and efficiently fully-discrete numerical approximation for solving the thermodynamically consistent hydrodynamically coupled phase-field model to study fluid-structure interaction in an irregular domain. The newly proposed algorithm is second-order accurate both in time and space. The numerical scheme is proved to inherit the original energy stable, which is also further verified numerically through several examples. In addition, the computation in each time step is significantly cheaper, and it is straightforward to program because several linear systems require to be solved except for the calculations of the supplementary variables. Thanks to the paradigm for the SVM, we can adopt an augmented Lagrangian approach to solve the supplementary variables efficiently so that the calculating amount is more minimal

than the total cost within a time step. Finally, the numerical experiments indicated that the proposed scheme achieved desired accuracy and energy dissipation properties and performed well in the complex fluid environment. The proposed numerical framework could be applied to investigate other phase-field hydrodynamics models for quasi-incompressible fluids and complex fluids.

Acknowledgements

Qi Hong's research is partially supported by the National Natural Science Foundation of China (Grant No. 12201297) and the LCP Fund for Young Scholar (Grant No. 6142A05QN22005). Yuezheng Gong's research is partially supported by the Foundation of Jiangsu Key Laboratory for Numerical Simulation of Large Scale Complex Systems (Grant No. 202002), the Fundamental Research Funds for the Central Universities (Grant No. NS2022070), the Natural Science Foundation of Jiangsu Province (Grant No. BK20220131) and the National Natural Science Foundation of China (Grant No. 12271252). Jia Zhao's research is partially supported by the National Science Foundation (NSF) USA with DMS-2111479.

References

- [1] F. Boyer and S. Minjeaud. Numerical schemes for a three component Cahn-Hilliard model. *ESAIM: Math. Model. Numer. Anal.*, 45:697–738, 2011.
- [2] M. Brassel and E. Bretin. A modified phase field approximation for mean curvature flow with conservation of the volume. *Math. Methods Appl. Sci.*, 34:1157–1180, 2011.
- [3] A. Bray. Theory of phase-ordering kinetics. Adv. Phys., 43:357–459, 1994.
- [4] J. Butcher. Numerical Methods for Ordinary Differential Equations. John Wiley & Sons, 2016.
- [5] J. Cahn and J. Hilliard. Free energy of a nonuniform system. I. interface free energy. *J. Chem. Phys.*, 28:258–267, 1958.
- [6] Y. Cai and J. Shen. Error estimates for a fully discretized scheme to a Cahn-Hillirad Phase-field models for two-phase incompressible flows. *Math. Comput.*, 87:2057–2090, 2018.
- [7] L. Chen. Phase-field modeling for microstructure evolution. *Annu. Rev. Mater. Res.*, 32:113–140, 2002.
- [8] W. Chen, W. Feng, Y. Liu, C. Wang, and S. Wise. A second order energy stable scheme for the Cahn-Hilliard-Hele-Shaw equation. *Discrete Contin. Dyn. Syst. B*, 24(1):149–182, 2019.
- [9] W. Chen, D. Han, C. Wang, S. Wang, X. Wang, and Y. Zhang. Error estimate of a decoupled numerical scheme for the Cahn-Hilliard-Stokes-Darcy system. *IMA J. Numer. Anal.*, 42(3):2621–2655, 2022.
- [10] W. Chen, Y. Liu, C. Wang, and S.M. Wise. Convergence analysis of a fully discrete finite difference scheme for Cahn-Hilliard-Hele-Shaw equation. *Math. Comput.*, 85:2231–2257, 2016.
- [11] W. Chen, C. Wang, S. Wang, X. Wang, and S. Wise. Energy stable numerical schemes for ternary Cahn-Hilliard system. *J. Sci. Comput.*, 84:27, 2020.
- [12] Y. Chen and J. Shen. Efficient, adaptive energy stable schemes for the incompressible Cahn-Hilliard Navier-Stokes phase-field models. *J. Comput. Phys.*, 308:40–56, 2016.
- [13] Q. Cheng, C. Liu, and J. Shen. A new Lagrange multiplier approach for gradient flows. *Comput. Methods Appl. Mech. Engrg.*, 367:113070, 2020.
- [14] L. Dong, C. Wang, S. Wise, and Z. Zhang. A positive-preserving, energy stable scheme for a ternary Cahn-Hilliard system with the singular interfacial parameters. *J. Comput. Phys.*, 442:110451, 2021.
- [15] Q. Du, L. Ju, X. Li, and Z. Qiao. Maximum principle preserving exponential time differencing schemes for the nonlocal Allen-Cahn equation. *SIAM J. Numer. Anal.*, 57:875–898, 2019.
- [16] Q. Du, L. Ju, X. Li, and Z. Qiao. Maximum bound principles for a class of semilinear parabolic equation and exponential time differencing schemes. *SIAM Rev.*, 63:317–359, 2021.
- [17] Q. Du, C. Liu, R. Pyham, and X. Wang. Phase field modeling of the spontaneous curvature effect in cell membranes. *Commun. Pure Appl. Math.*, 4:537–548, 2005.
- [18] A. E. Eiegel, C. Wang, X. Wang, and S.M. Wise. Convergence analysis and error estimates for a second order accurate finite element method for the Cahn-Hilliard-Navier-Stokes system. *Numer. Math.*, 137:495–534, 2017.

- [19] Y. Gong, Q. Hong, and Q. Wang. Supplementary variable method for thermodynamically consistent partial differential equations. *Comput. Methods Appl. Mech. Engrg.*, 381:113746, 2021.
- [20] F. Guillen-Gonzailez and G. Tierra. Splitting schemes for a Navier-Stokes model for two fluids with different densities. *J. Comput. Math.*, 32:643–664, 2014.
- [21] Z. Guo, P. Lin, J. Lowengrub, and S. Wise. Mass conservative and energy stable finite difference methods for the quasi-incompressible Navier-Stokes-Cahn-Hilliard system: primitive variable and projection-type schemes. *Comput. Methods Appl. Mech. Engrg.*, 326:144–174, 2017.
- [22] E. Hairer, C. Lubich, and G. Wanner. *Geometric Numerical Integration: Structure-Preserving Algorithms for Ordinary Differential Equations*, volume 31. Springer, 2006.
- [23] Q. Hong, J. Li, and Q. Wang. Supplementary variable method for structure-preserving approximations to partial differential equations with deduced equations. *Appl. Math. Lett.*, 110:106576, 2020.
- [24] J.J. Huang and L. Zhang. Simplified method for wetting on curved boundaries in conservative phase-field lattice-Boltzmann simulation of two-phase flows with large density ratios. *Phys. Fluids*, 34:082101, 2022.
- [25] D. Jeong, J. Yang, and J. Kim. A practical and efficient numerical method for the Cahn-Hilliard equation in complex domains. *Commun. Nonlinear Sci. Numer. Simul.*, 73:217–228, 2019.
- [26] X. Jing, J. Li, X. Zhao, and Q. Wang. Second order linear energy stable schemes for Allen-Cahn equations with nonlocal constraints. *J. Sci. Comput.*, 80:500–537, 2019.
- [27] J. Kim and J. Lowengrub. Phase field modeling and simulation of three-phase flows. *Interfaces Free Bound.*, 7:435–466, 2005.
- [28] H. Lee and J. Kim. Accurae contact angle boundary conditions for the Cahn-Hilliard equations. *Comput. Fluids*, 44:178–186, 2011.
- [29] D. Li, Z. Qiao, and T. Tang. Characterizing the stabilization size for semi-implicit Fourier-spectral method to phase field equations. *SIAM J. Numer. Anal.*, 54:1653–1681, 2016.
- [30] Y. Li, J. Choi, and J. Kim. Multi-component Cahn-Hilliard system with different boundary conditions in complex domains. *J. Comput. Phys.*, 323:1–16, 2016.
- [31] Y. Li and J. Kim. Multiphase image segmentation using a phase-field model. *Comput. Math. Appl.*, 62:737–745, 2011.
- [32] L. Lin, X. Liu, and S. Dong. A gPAV-based unconditionally energy-stable scheme for incompressible flows with outflow/open boundaries. *Comput. Methods Appl. Mech. Engrg.*, 365:112969, 2020.
- [33] J. Lober, F. Ziebert, and I. Aranson. Collisions of deformable cells leads to collective migration. *Sci. Rep.*, 5:9172, 2015.
- [34] J. Lowengrub, A. Ratz, and A. Voigt. Phase-field modelling of the dynamics of multicomponent vesicles: spinodal decomposition, coarsening, budding, and fission. *Phys. Rev. E*, 79:031926, 2009.
- [35] S. Mitra, M.J. Sathe, E. Doroodchi, R. Utikar, M.K. Shah, V. Pareek, J.B. Joshi, and G.M. Evans. Droplet impact dynamics on a spherical particle. *Chem. Eng. Sci.*, 100:105–119, 2013.
- [36] J. Rubistein and P. Sternberg. Nonlocal reaction-diffusion equations and nucleation. *IMA J. Appl. Math.*, 48:249–264, 1992.
- [37] D. Shao, W. Pappel, and H. Levine. Computational model for cell morphodynamics. *Phys. Rev. Lett.*, 105:108104, 2010.
- [38] J. Shen, J. Xu, and J. Yang. The scalar auxiliary variable (SAV) approach for gradient flows. *J. Comput. Phys.*, 353:407–416, 2018.
- [39] J. Shen and X. Yang. Numerical Approximations of Allen-Cahn and Cahn-Hilliard Equations. *Discrete Contin. Dyn. Syst.*, 28:1669–1691, 2010.
- [40] J. Shen and X. Yang. Decoupled, energy stable schemes for phase-field models of two-phase incompressible flows. *SIAM J. Numer. Anal.*, 53:279–296, 2015.
- [41] L. Shen, Z. Xu, P. Lin, H. Huang, and S. Xu. A energy stable C^0 finite element scheme for a phase-field model of vesicle motion and deformation. *SIAM J. Sci. Comput.*, 44:B122–B145, 2022.
- [42] J. Shin, D. Jeong, and J. Kim. A Conservative numerical method for the Cahn-Hilliard equation in complex domains. *J. Comput. Phys.*, 230:7441–7455, 2011.
- [43] C. Wang and S. Wise. A thermodynamically-consistent phase field crystal model of solidification with heat flux. *Journal of Mathematical Study*, 55:337–357, 2022.
- [44] Q. Wang. *Generalized Onsager Principle and its Application*. Froniter and Progress of Current Soft Matter Research, Springer Nature, 2020.
- [45] X. Wang and Q. Du. Modeling and simulations of multi-component lipid membranes and open membranes via diffuse interface approaches. *J. Math. Biol.*, 56:347–371, 2008.
- [46] S. Wise. Unconditionally stable finite difference nonlinear multigrid simulation of the Cahn-

- Hilliard-Hele-Shaw system of equations. J. Sci. Comput., 44:38-68, 2010.
- [47] C. Xu and T. Tang. Stability analysis of large time-stepping methods for epitaxial growth models. *SIAM J. Numer. Anal.*, 44(4):1759–1779, 2006.
- [48] J. Xu, Y. Li, S. Wu, and A. Bousquet. On the stability and accuracy of partially and fully implicit schemes for phase field modeling. *Comput. Methods Appl. Mech. Engrg.*, 345:826–853, 2019.
- [49] X. Xu, Y. Di, and H. Yu. Sharp-interface limits of a phase-field model with a generalized Navier slip boundary condition for moving contact lines. *J. Fluid Mech.*, 849:805–833, 2018.
- [50] J. Yang, J. Wang, and J. Kim. Energy-stable method for the Cahn-Hilliard equation in arbitrary domains. *Int. J. Mech. Sci.*, 228:107489, 2022.
- [51] X. Yang. Efficient, second-order in time, and energy estable scheme for a new hydrodynamically coupled three components volume-conserved Allen-Cahn phase-field model. *Math. Models Methods Appl. Sci.*, 31:753–787, 2021.
- [52] X. Yang and X. He. A fully-discrete decoupled finite element method for the conserved Allen-Cahn type phase-field model of three-phase fluid flow system. *Comput. Methods Appl. Mech. Engrg.*, 389:76M10, 2022.
- [53] X. Yang, J. Zhao, and Q. Wang. Numerical approximations for the molecular beam epitaxial growth model based on the invariant energy quadratization method. *J. Comput. Phys.*, 333:104–127, 2017.
- [54] Z. Yang and S. Dong. An unconditionally energy-stable scheme based on implicit auxiliary energy variable for incompressible two-phase flows with different densities involving only precomputable coefficient matrices. *J. Comput. Phys.*, 393:229–257, 2019.
- [55] Z. Yang and S. Dong. A roadmap for discretely energy-stable schemes for dissipative systems based on a generalized auxiliary variable with guaranteed positivity. *J. Comput. Phys.*, 404:109121, 2020.
- [56] M. Yuan, W. Chen, C. Wang, S. Wise, and Z. Zhang. An energy stable finite element scheme for the three-component Cahn-Hilliard-type model for macromolecular microsphere composite hydrogels. *J. Sci. Comput.*, 87:78, 2021.
- [57] J. Zhao and D. Han. Second-order decoupled energy-stable schemes for Cahn-Hilliard-Navier-Stokes equations. *J. Comput. Phys.*, 443:110536, 2021.
- [58] J. Zhao, Y. Shen, M. Happasalo, Z. J. Wang, and Q. Wang. A 3D numerical study of antimicrobial persistence in heterogeneous multi-species biofilms. *J. Theor. Biol.*, 392:83–98, 2016.
- [59] J. Zhao, H. Yu, Q. Wang, and X. Yang. A linearly decoupled energy stable scheme for phase field models of three-phase incompressible viscous fluid flows. *J. Sci. Comput.*, 2016.
- [60] Y. Zhao, Y. Ma, H. Sun, and Q. Du. A new phase-field approach to variational implicit solvation of charged molecules with the Coulomb-field approximation. *Commun. Math Sci.*, 16:1203–1223, 2018.
- [61] C. Zhou, P. Yue, J. Feng, C. Olliver-Gooch, and H.H. Hu. 3D phase-field simulations of interfacial dynamics in newtonian and viscoelastic fluids. *J. Comput. Phys.*, 229:498–511, 2010.

Journal Pre-proof

oxtimes The authors declare that they have no known competing financial interests or personal relationships that could have appeared to influence the work reported in this paper.
\Box The authors declare the following financial interests/personal relationships which may be considered as potential competing interests: